Study of Trileptonic Final States with High Transverse Momenta at H1

Diploma Thesis

submitted by
Dieter Bachmann

supervisor
Prof. Dr. R. Eichler

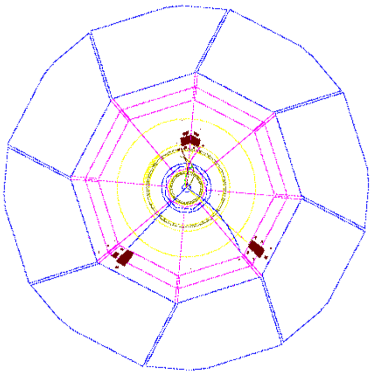

July 1998
Institute for Particle Physics, ETH Zürich

Erwarte nicht / Das dreimal glühende Licht!
Goethes Faust, Z.1318/9

Zusammenfassung

Das Massenspektrum von trileptonischen Endzuständen bei hochenergetischer Positron-Proton-Streuung, $ep \to eeeX$, bestimmt anhand der von H1 während der Jahre 1994-1997 akkumulierten Daten, ist in Übereinstimmung mit den Vorhersagen von Monte-Carlo-Simulationen, die sowohl Bethe-Heitler- als auch Compton-Graphen in Betracht ziehen. Für transversale Impulse von $p_{\perp 1} > 10\,\mathrm{GeV}$ und $p_{\perp 2} > 5\,\mathrm{GeV}$ für beliebige zwei Leptonen des Endzustandes ergibt sich für den sichtbaren Winkelbereich der Wirkungsquerschnitt $\sigma^{\mathrm{vis}}_{ep \to eeeX} = \left(1.17 \pm 0.19^{+0.21}_{-0.27}\right)\,\mathrm{pb}$, während $\sigma^{\mathrm{vis,\ MC}}_{ep \to eeeX} = 1.47\,\mathrm{pb}$ von Monte-Carlo erwartet wird.

Abstract

The mass spectrum of trileptonic final states of high energy positron-proton scattering is determined from H1 1994 to 1997 data and is found to be in agreement with Monte-Carlo simulation of Bethe-Heitler and Compton graphs. For transverse momenta $p_{\perp 1} > 10\,\mathrm{GeV}$ and $p_{\perp 2} > 5\,\mathrm{GeV}$ for any two of the final state leptons, the cross-section is calculated for the visible angular range to $\sigma^{\mathrm{vis}}_{ep \to eeeX} = \left(1.17 \pm 0.19^{+0.21}_{-0.27}\right)\,\mathrm{pb}$ while $\sigma^{\mathrm{vis,\ MC}}_{ep \to eeeX} = 1.47\,\mathrm{pb}$ is expected by Monte-Carlo simulation.

Contents

Chapter 1

Introduction

This analysis is concerned with the generation of *ee* pairs by *ep*-collision at the HERA storage ring of DESY Foundation in Hamburg. The data examined includes data collected by the H1 experiment during the years 1994-1997, amounting to an integrated luminosity of 36.3 pb. Lepton pairs are dominantly produced through two-photon-processes. In addition to these, resonances may occur at energies that correspond to the mass of a heavy particle, such as a heavy quark bound state or the Z^0 vector boson.

This introductory chapter has the aim of making the text more self-contained. It supplies a short review of some facts about the Standard Model and standard definitions in particle physics. In section 1.4, a brief motivation for the present analysis is given.

1.1 Kinematics of Electron-Proton Scattering

Consider the collision of an electron with a proton represented in the picture below. The incoming electron's 4-momentum is k_μ, the scattered one's is k'_μ. The transferred momentum is $q_\mu = (k'_\mu - k_\mu)$. The incoming proton has a 4-momentum of p_μ and is fragmented into n remnant particles (set $n = 1$ for elastic scattering) with 4-momenta $p_\mu^{1..n}$.

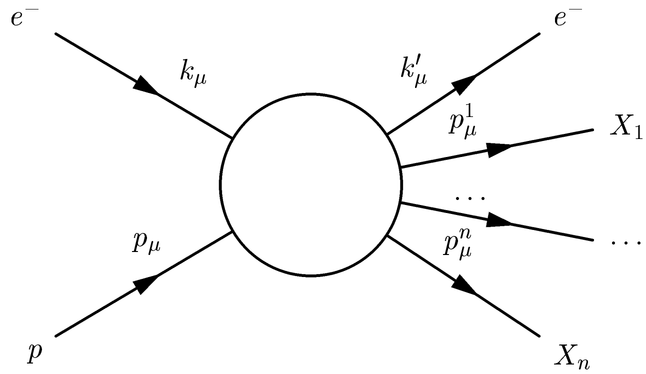

While in the case of elastic scattering, one scalar variable alone (e.g. q^2) is sufficient to describe event kinematics, the fragmentation of the proton in inelastic scattering involves additional degrees of freedom, so that 3 variables are needed for a description. Out of the following standard definitions of scalars:

$$\begin{aligned}
x &= \frac{-q^2}{2p_\mu q^\mu}, \quad 0 \leq x \leq 1 \\
y &= \frac{p_\mu q^\mu}{p_\mu k^\mu}, \quad 0 \leq y \leq 1 \\
s &= (k_\mu + p_\mu)^2 \\
t &= (k'_\mu - k_\mu)^2 = q^2 \\
u &= \left(k_\mu - \sum p^i_\mu\right)^2 \\
Q^2 &= -q^2 = -t
\end{aligned}$$

one choice would be (s, x, y). x and y are called the *Bjorken variables*, s, t and u are the *Mandelstam variables.* The physical interpretation of these quantities is as follows: In a parton model, x represents the fraction of proton momentum carried by the proton constituent participating in the scattering. y is the fraction of energy lost by the electron in the system of the resting proton, $\sqrt{s}$ is the center-of-mass energy and $t = q^2 = -Q^2$ is the transferred momentum squared, so that $Q^2 \to xys$ for momenta large in comparison to particle masses.

1.2 The Standard Model and New Physics

The Standard Model accounts for the three known non-gravitational interactions and for all known particles. These include 6 quarks (strongly interacting) and 6 leptons (not strongly interacting) as well as four types of gauge bosons mediating the interactions, not counting the respective anti-particles (c.f. figure 1.1).

All of these particles have by now been seen [1], and they would complete the Standard Model but for the postulation of the undiscovered $Higgs-particle$ that would account for the masses of the W and Z gauge-bosons by means of spontaneous symmetry-breakdown (SSB), uniting the electromagnetic (γ) and weak (W, Z) interactions (Glashow, Salam, Weinberg, 1967).

The logical structure of the Standard Model is to postulate existence of the known fermions with their respective masses and to require local gauge invariance, thereby generating the gauge bosons. The gauge groups SU(3)⊗SU(2)⊗U(1) generate strong, weak and electromagnetic interactions

quarks		leptons		gauge-bosons
$q = +2/3$	$q = -1/3$	$q = -1$	$q = 0$	e.m., weak & strong forces
u (up)	d (down)	e^- (electron)	ν_e	γ (photon)
c (charm)	s (strange)	μ^- (muon)	ν_μ	$Z^0, W^\pm$
t (top/truth)	b (bottom/beauty)	τ^- (tau)	ν_τ	g_{ij} (gluons)

Table 1.1: *Known particles sorted by spin and charge. Not included are fermionic anti-particles. Both quarks and gluons carry colour ("strong charge") and come in three and eight varieties, respectively.*

respectively. The notation as a direct product alludes to the hope to unify these groups in one supergroup and thus explain the three interactions as the spontaneously broken version of one gauge interaction (Grand Unified Theory, GUT). The chief candidate for this is supersymmetry (SUSY), linking fermions and bosons. No, or very inconclusive, experimental evidence for supersymmetry has been found [2]. As SUSY introduces a host of new particles and interactions, resonances would become visible at the corresponding (possibly very high) energies which would induce a breakdown of the Standard Model. No scientific world-views, not even aesthetically pleasing ones like Newton's, have been subjected to equally enormous efforts towards their deconstruction without exhibiting any noticeable flaw as has been the case with the direct sum (Standard Model $\oplus$ General Relativity), so that empirically, not conceptually, the Standard Model is the best theory available.

It has become clear that possession of a theory is far from being equivalent to the understanding of that theory. The Standard Model would be working as well without the concept of spontaneous symmetry breakdown or indeed the general proof of its renormalisability (t'Hooft, 1971). In this sense, discovery of SSB has been a promising example of how an empirically sound theory can later turn out to be more aesthetically pleasing than was at first evident.

In spite of this, the first experimental step towards a conceptually satisfying physical world-picture boils down to the mission to *find any failure of the Standard Model.*

1.3 Cross-Sections

A short review of the definition of a cross-section is given as a reminder of the origin of the predicted values that measured quantities are going to be compared with. See chapters 3 and 6 of Weinberg's book [3] for more details.

1.3.1 S-Matrix and Invariant Amplitudes

The probability amplitude for the transition of some initial state $|\alpha\rangle$ into some final state $|\omega\rangle$ is the scalar product

$$S_{\omega\alpha} = \langle\alpha|\omega\rangle\,.$$

This array of complex amplitudes is known as the *S-Matrix*, $|\omega\rangle = S\,|\alpha\rangle$; the rate of a reaction $|\alpha\rangle \to |\omega\rangle$ is proportional to $|S_{\omega\alpha} - \delta(|\alpha\rangle - |\omega\rangle)|^2$. S is connecting two complete sets of orthonormal states, and because of the completeness relation it must be unitary:

$$\int \mathrm{d}\beta\, S^*_{\beta\gamma} S_{\beta\alpha} = \int \mathrm{d}\beta\, \langle\gamma_{t\to\infty}|\beta_{t\to-\infty}\rangle\,\langle\beta_{t\to-\infty}|\alpha_{t\to\infty}\rangle = \delta(\gamma-\alpha)$$

i.e. $S^\dagger S = SS^\dagger = 1$. S exhibits all symmetries of the theory, notably Lorentz invariance and CPT-symmetry, and it enforces 4-momentum conservation by a $\delta(p_\omega - p_\alpha)$ term. The delta-function-free part of S is called the *Invariant Amplitude M*:

$$S_{\omega\alpha} = -2i\pi\delta(p_\omega - p_\alpha)M_{\omega\alpha}.$$

The *transition rate* dΓ of a given process is the transition probability per unit time; for two particles in initial state, enclosed in a macroscopic volume V, this is

$$\mathrm{d}\Gamma(|\alpha\rangle \to |\omega\rangle) = (2\pi)^4 V^{-1} |M_{\omega\alpha}|^2 \delta^4(p_\omega - p_\alpha)\mathrm{d}\omega.$$

The rate is proportional to V^{-1}, that is the density of either particle at the position of the other one. The *flux* Φ of either particle at the position of the other one is the product of particle density and relative velocity,

$$\Phi_\alpha = u_\alpha/V; \quad u_\alpha = \frac{\sqrt{(p_1\cdot p_2)^2 - m_1^2 m_2^2}}{E_1 E_2}.$$

Finally, the differential *cross-section* of the process is defined as the transition rate per flux,

$$\mathrm{d}\sigma = \mathrm{d}\Gamma(|\alpha\rangle \to |\omega\rangle)/\Phi_\alpha = (2\pi)^4 u_\alpha^{-1} |M_{\omega\alpha}|^2 \delta^4(p_\omega - p_\alpha)\mathrm{d}\omega.$$

It has the dimension of an area.

1.3.2 Perturbation Theory

If the interaction is expressed by means of a Hamiltonian $H_1(t)$, access to perturbative calculation of S is provided by the *Dyson series*

$$S = \mathrm{T}\ \exp\left(-i\int_{-\infty}^{\infty} \mathrm{d}t\ H_1(t)\right)$$

(Dyson 1949) where the time ordering operator T indicates ordering of each term in the series expansion. Dyson's approach makes use of the diagrammatic technique proposed by Feyman in a path-integral context at the 1948 Poconos Conference with the invaluable advantage of manifest Lorentz covariance. The structure of a specific Feynman diagram visualizes the pairing of the interaction Hamiltonians in the corresponding series term. Again, see [3].

1.3.3 Visible Cross-Sections

Calculated cross-sections provide a direct link of quantum field theory with experiment: The cross-section of any process is directly proportional to the number of events observed. Cross-sections are areas, and a convenient unit in the present context is the *picobarn*, $1\,\mathrm{pb} = 10^{-40}\mathrm{m}^2$. The integrated luminosity L of an experiment is simply the number of events N accumulated per unit area cross-section, so that $\sigma = N/L$.

Now the cross-section has to be constrained to regions of phase-space visible to the detector (angular regions, minimal momenta etc.). Also, the efficiency ε of actual reconstruction of an occurred event by the complex ensemble of hardware and software has to be carefully determined, so that finally the visible cross-section is

$$\sigma_{\mathrm{vis}} = \frac{N}{\varepsilon \cdot L}.$$

1.4 Motivation of this Analysis

1.4.1 High-Q^2-Events at H1

Events with high momentum transfer are sparse. Yet the luminosity accumulated by HERA over the years allows analysis up to values of $Q^2 \approx 10^4\,\mathrm{GeV}^2$. In 1997, analysis of the 1994-1996 data seemed to exhibit an excess of high Q^2-events over the values predicted by the Standard Model for both neutral current (NC, exchange of an uncharged gauge boson) and charged current (CC, exchange of a charged W boson) processes [4]. Statistics were low indeed, but hopes were high that these observations were heralding the impending collapse of the Standard Model [5],[6]. Unfortunately, 1997 data does not appear to be backing these trends and the excesses have been swamped by increased statistics rather than amplified, so chances are that the effect had been due to statistical fluctuation. However, also the decrease of the effect could be such, and it is still conceivable that there are new particles just out of reach.

1.4.2 Trileptonic Final States

W-production with leptonic W-decay, $ep \to ee\nu_e X$ is difficult to distinguish from pair production $ep \to eeeX$ with one e undetected. The generated neutrino will tend to carry away transverse momentum that will appear to be "missing". An analysis of events with high energy leptons and missing transverse momentum has found an excess over expectation [7]. The purpose of this analysis is to see if such an excess is also found in pair production events, i.e. events with low missing transverse momentum.

The dominant contribution to the production of lepton pairs are from two-photon-processes. The cross-section of these diverges for low invariant masses of the generated pair, rending simulation impracticable. Therefore, events with high invariant mass pairs or with high $p_\perp$ particles should be looked for. Resonances from heavy quark productions do not play a rôle in this analysis because the high threshold imposed on particle transverse momenta suppresses these (except for the $t\bar{t}$ resonance which at some 350 GeV is out of reach for HERA).

1.4.3 Pair Invariant Mass

The aim of this analysis is to plot the spectrum of invariant mass of the generated leptons. The invariant mass of a four-vector is a Lorentz scalar:

$$m(p_\mu) = p^\mu p_\mu = E^2 - p_x^2 - p_y^2 - p_z^2.$$

Thus, if a resonant particle decays into several daughter particles, the sum of their 4-momenta still yields the original invariant mass, $m_{123\ldots} = m(p_\mu^1 + p_\mu^2 + p_\mu^3 \ldots)$.

Since we have an e present already in the initial state, and since an e in the final state cannot be determined to be either a scattered or a generated particle, the invariant mass is taken of whichever two leptons have a sufficiently high transverse momenta to show up in the calorimeter. Only in a very few cases three leptons are detected. These events are treated seperately and are represented in the appendix.

1.4.4 A Word on Muons

Only the first lepton generation (e) is at all considered in this analysis. Higher generation leptons have higher masses and as a consequence they have a finite lifetime, decaying into lighter particles. Apart from this, they have exactly the same properties as first generation leptons. While the τ lepton has too short a mean life to allow direct detection (even at $E_\tau \approx$ 100 GeV, a τ will only travel a few cm), an analysis of μ pair production $ep \to e\mu\mu X$ is perfectly feasible, and has indeed been performed for 1994 data [24]. Because the generated particles are distinguishable from the incident lepton, the combinatorical problem of which final state leptons to pair does not arise and also there will be no contribution from crossed graphs. Other impediments emerge though, notably background from cosmic muons. A new analysis is in preparation [18].

Chapter 2

DESY, HERA and H1

DESY (*Deutsches Elektronen-Synchrotron*) was founded in 1959. Today, some 2600 scientists from 280 universities in 35 countries are doing research at DESY. H1 has some 410 members from 37 institutes in 11 countries. See table 2.1 for historical details.

2.1 The HERA Storage Ring

HERA (Hadron Electron Ring Accelerator) is situated in Hamburg, Germany. Electrons and protons are accelerated in opposing directions in two independent storage rings at 27.5 GeV and 820 GeV respectively for the benefit of four physics experiments – H1 to the north and ZEUS to the south working with colliding beams, and HERMES to the east and HERA-B to the west, both operating in fixed target mode (c.f. figure 2.1).

Older storage rings, DESY II, DESY III and PETRA (Positron Electron Tandem Ring Accelerator) are used for the injection of electrons and protons at 12 GeV and 40 GeV respectively. Table 2.3 lists the preaccelerators used for HERA together with their length/circumference and the type of particles accelerated. In 1995, lepton beam polarity has been reversed in order to maximize beam lifetime, so for most of the data looked at for this analysis (96%), protons have been colliding with positrons rather than electrons. See table 2.2 for mean currents attained by HERA.

2.2 The H1 Detector

The H1 detector is described in detail in reference [8]. H1 (as well as ZEUS) was built to enable measurement of the proton structure function in deep inelastic scattering and more generally to explore new regions of phase space in the hope of discovery of unknown particles. H1's size is approximately $x \times y \times z = 12\,\mathrm{m} \times 14\,\mathrm{m} \times 10\,\mathrm{m}$ at a mass of 2800 metric tons. It has been commissioned in spring 1992.

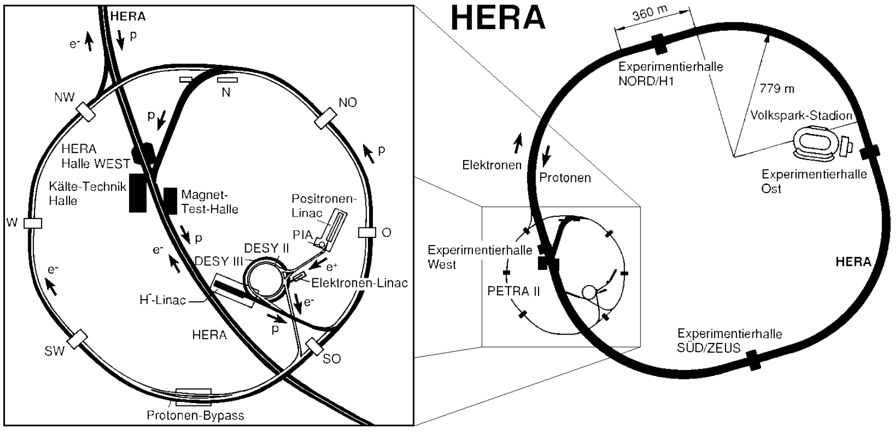

year of commissioning	1992
circumference	6336 m
particle bunch number	210
bunch crossing time	96 ns
max. center of mass energy	$\sqrt{s} = 314\,\mathrm{GeV}$
max. luminosity	$1.5 \cdot 10^{31}\,\mathrm{cm}^{-2}\mathrm{s}^{-1} = 15\,\mathrm{mb}^{-1}\mathrm{s}^{-1}$

Figure 2.1: *the HERA storage ring*

1959	Desy Foundation established on December 18th in Hamburg
1960-1964	construction of the electron synchrotron DESY
1964	commissioning of electron linear accelerator LINAC I
1969	commissioning of positron linear accelerator LINAC II
1969-1974	construction of the double storage ring DORIS
1976-1978	construction of the $e^{\pm}$ tandem ring accelerator PETRA
1979	discovery of the gluon at PETRA
1984-1990	construction of the hadron-electron ring accelerator HERA
1987	commissioning of the electron synchrotron DESY II
1988	commissioning of the H^{-}/p linear accelerator LINAC III and the proton synchrotron DESY III
1988-1992	assembly of the HERA detectors H1 and ZEUS
1990	commissioning of PETRA as preaccelerator for $e^{\pm}$ and p
1991	October 19th, first *ep* collisions in HERA
1992	start of particle physics experiments at HERA in June
1994-1995	assembly of the HERMES detector at HERA
1995	February, approval of HERA-B, the fourth experiment at HERA

Table 2.1: *History of DESY [9]*

year	$\langle I_e \rangle$ (mA)	$\langle I_p \rangle$ (mA)	L (pb^{-1})
1994	17.0	41.0	5.27
1995	18.4	54.0	9.94
1996	20.6	60.3	14.46
1997	28.2	73.5	33.36

Table 2.2: *HERA 1994-1997: mean beam currents and delivered integrated luminosity.*

accelerator	particles	energy	length
LINAC II	$e^{\mp}$	450 MeV	70 m
LINAC III	p	50 MeV	32 m
PIA	$e^{\mp}$	450 MeV	29 m
DESY II	$e^{\mp}$	8 GeV	293 m
DESY III	p	7.5 GeV	317 m
PETRA II	$e^{\mp}/p$	12 GeV/40 GeV	2304 m

Table 2.3: *Type of particle accelerated, energy attained and length/circumference for the preaccelerators used for HERA [9]*

The coordinate system is defined as shown in figure 2.2: The positive z axis is pointing in the direction of the proton beam, y skywards, x to the ring center, $\theta = 0$ points in positive z-direction, $\phi = 0$ in direction of positive x .

Due to the imbalanced distribution of beam energies, generated particles will be scattered predominantly into the forward region. This has motivated an asymmetric design of the detector with a superior instrumentation of the forward region (direction of the center of mass system).

2.2.1 Calorimetry

An overview over calorimeter properties is given in table 2.4. Solely calorimeters relevant to this analysis are referred to here. Not treated are the system for muon detection (muon chamber, instrumented iron) and the forward detector (PLUG).

Liquid Argon (LAr)

The liquid argon calorimeter is designed to provide high position and energy resolution. Its inner section, the *electromagnetic* one (ECAL), is composed of lead absorbers and gaps filled with liquid argon allowing the detection of electromagnetic showers ($\gamma, e^{\mp}$) at a resolution of $4 \times 8\,\mathrm{cm}^2$. The outer,

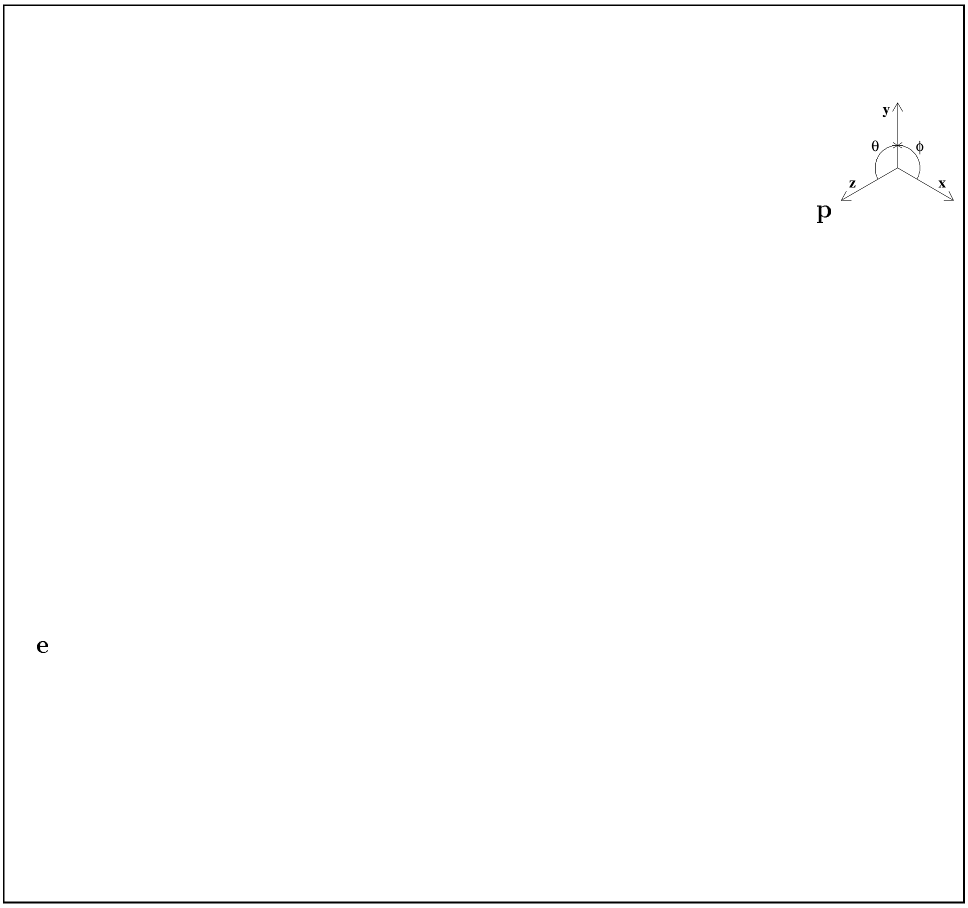

1	Beam pipe and beam magnets	9	Muon chambers
2	Central tracking device	10	Instrumented iron yoke
3	Forward tracking device	11	Forward muon toroid
4	Electromagnetic LAr calorimeter	12	Spaghetti calorimeter (SpaCal)
5	Hadronic LAr calorimeter	13	PLUG calorimeter
6	Superconducting coil (1.15 T)	14	Concrete shielding
7	Compensating magnet	15	Liquid argon cryostat
8	Helium supply for 7		

Figure 2.2: *Overview of H1. The coordinate system is represented in the top right corner.*

calorimeter	θ range	granularity	$\sigma(E)/E$
LAr (e.m.)	$4^\circ - 154^\circ$	$10 - 100\,\mathrm{cm}^2$	$(11\%/\sqrt{E}) \oplus 1\%$
LAr (hadr.)	$4^\circ - 154^\circ$	$50 - 2000\,\mathrm{cm}^2$	$(50\%/\sqrt{E}) \oplus 2\%$
SpaCal	$151^\circ - 176^\circ$	$4 \times 4\,\mathrm{cm}^2$	$(7.1\%/\sqrt{E}) \oplus 1\%$
BEMC	$151^\circ - 176^\circ$	$16 \times 16\,\mathrm{cm}^2$	$(10\%/\sqrt{E}) \oplus 17\%$
Tagger	$> 179.7^\circ$	$2.2 \times 2.2\,\mathrm{cm}^2$	$(10\%/\sqrt{E}) \oplus 1\%$

Table 2.4: *Calorimeter properties: angular range, granularity, energy resolution; the sign $\oplus$ signifies quadratic summation.*

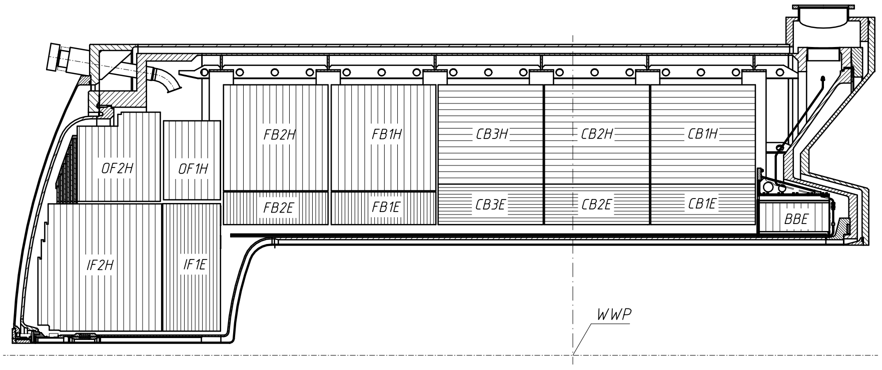

Figure 2.3: *Cross section of the LAr calorimeters; WWP marks the interaction point (*Wechselwirkungspunkt*). The calorimeter names refer to their position: IF, OF for inner and outer forward region, FB, CB, BB for forward, central and backward barrels. the letters H or E refer to hadronic or e.m. sections.*

hadronic section (HCAL) has absorbers of stainless steel and a pad size of $8 \times 8\,\mathrm{cm}^2$.

Spaghetti Calorimeter (SpaCal)

Since 1995, the SpaCal is covering the backward region of H1. Both its electromagetic and hadronic sections are composed of scintillating fibres embedded in a lead matrix [11],[12].

SpaCal was inserted during shutdown 1994/5, replacing the BEMC, a lead-copper sandwich calorimeter. The SpaCal features higher granularity (c.f. table 2.4) and enables improved triggering and timing. In spite of the hadronic section of SpaCal, both BEMC and SpaCal are too thin for reliable detection of hadronic showers.

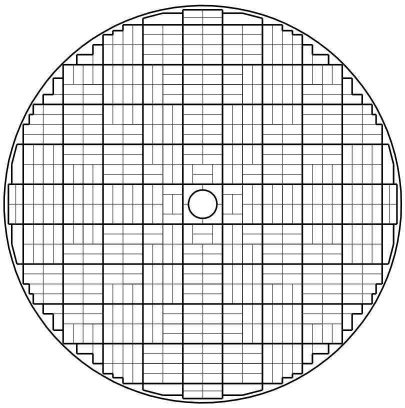

Figure 2.4: *Schematic $r\phi$-view of the SpaCal (electromagnetic section) showing submodules, units of two calorimeter cells of* $4 \times 4\,\mathrm{cm}^2$ *each (the total diameter is about* $1.6\,m$*).*

central	$25^\circ < \theta < 155^\circ$	$150 < r < 850\,\mathrm{mm}$
forward	$7^\circ < \theta < 25^\circ$	$150 < r < 750\,\mathrm{mm}$
backward	$155^\circ < \theta < 175^\circ$	$135 < r < 650\,\mathrm{mm}$

Table 2.5: *angular and radial ranges covered by the different tracking devices*

2.2.2 Tracking

The tracking system enables track triggering as well as particle reconstruction and identification. Its central, forward and backward detectors all contain layers of drift chambers and multiwire proportional chambers.

For the central region there are two concentric cylindrical drift chambers (CJC1, CJC2) with a resolution in the $r\phi$-plane of $\sigma_{r\phi} \approx 170\,\mu\mathrm{m}$. The z-coordinate of a hit is determined by division of charges measured at each end of the wire at a resolution of $\sigma_z \approx 2.2\,\mathrm{cm}$. See figure 2.5 for a radial view of the central tracking system.

For improved resolution in z, the central inner and outer z-chambers (CIZ, COZ) contain wires strung perpendicular to the beam axis. They attain a resolution of $\sigma_z \approx 300\,\mu\mathrm{m}$. For track reconstruction, track elements of CJC1, CJC2 and CIZ, COZ can be linked for optimal accuracy in reconstruction of longitudinal and transversal momentum components.

The backward drift chamber (BDC) covers the region of $153^\circ < \theta < 177.5^\circ$ and is used mostly for the reconstruction of the scattered electron. The forward tracking detector (FTD), covering angles of $5^\circ < \theta < 20^\circ$, is designed for an angular resolution of $\sigma_{\theta,\phi} < 1\,\mathrm{mrad}$. However, low efficiency in track identification results in a considerably poorer effective resolution.

The superconducting coil around the LAr generates a field of $1.15\,\mathrm{T}$ in z-direction, bending charged particles' paths. An overview of the tracking

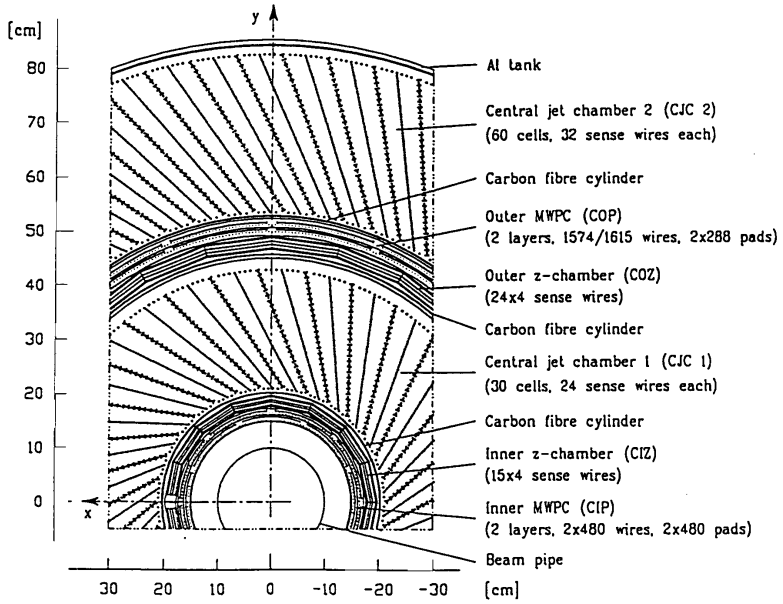

Figure 2.5: *xy-projection of the central tracking system showing the layers of central proportional-, jet- and z-chambers*

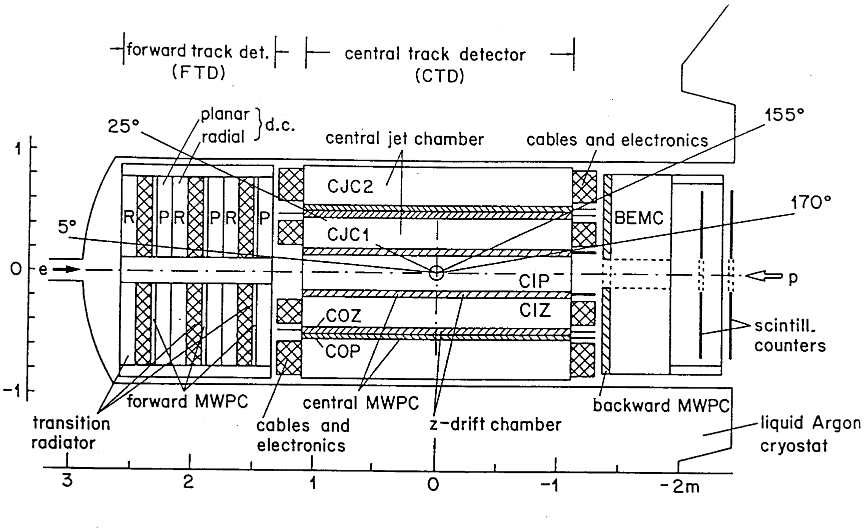

Figure 2.6: *side view of the H1 tracking system showing the positions of the various forward, central and backward tracking devices and their angular ranges*

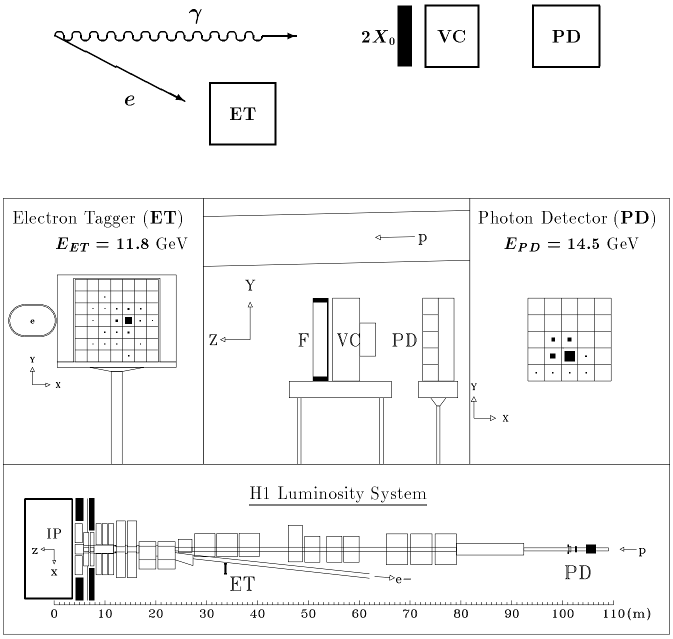

Figure 2.7: *the H1 luminosity system: schematic representation of the measured bremsstrahlung process, position of the detectors in the tunnel (center, bottom) and front view with response to a typical hit of the electron tagger (mid left) and photon detector (mid right).*

system is given in figure 2.6.

2.2.3 Luminosity

Luminosity is determined from the measurement of the bremsstrahlung (Bethe-Heitler [10]) process $ep \to ep\gamma$ (with a photon angle $\angle(\gamma, e)$ of less than $17\,\mu$rad). Background to this process stems mainly from remnant gas interaction $eA \to eA\gamma$ and is taken into account by observing electron pilot bunches (with the proton beam off) by means of the formula

$$L = \frac{R_{\text{tot}} - (I_{\text{tot}}/I_0)R_0}{\sigma_{\text{vis}}},$$

where σ_{vis} is the (known) visible cross-section of $ep \to ep\gamma$, R_{tot} is the total rate of the bremsstrahlung events, R_0 is the rate in the electron pilot bunches and I_{tot}, I_0 are the corresponding electron beam currents.

For the detection of both electron and photon involved in this process, respective detectors are placed close to the beam pipe, far along the tunnel (c.f. figure 2.7): The photon detector is placed at $-z = 103\,\text{m}$ from the interaction point, the electron tagger at $-z = 33\,\text{m}$. A second electron tagger

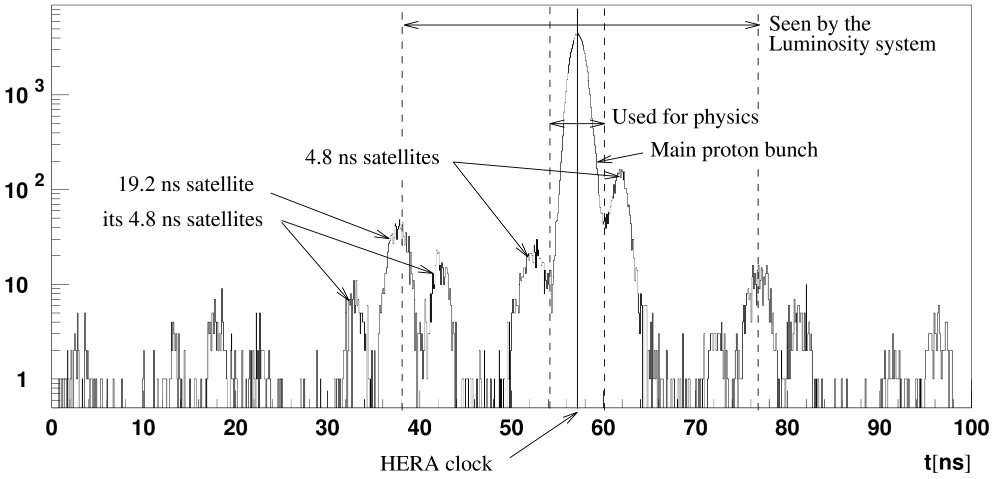

Figure 2.8: *Time spectrum of the proton beam as seen by the forward time-of-flight device (from [13]): Only events in a time window of* ± 3 *ns around bunch crossing time are used for physics.*

has been added during shutdown 1994/5, at $-z = 44\,\text{m}$ (c.f. [26]). Luminosity can be determined by means of the known cross-sections visible to these detectors ($23\,mb$ to the tagger at $33\,\text{m}$, $174\,\text{mb}$ to the photon detector).

2.2.4 Trigger

Only a small fraction of the events occurring inside the detector will be of physical interest. The task of the trigger system is to suppress recording of soft *ep*-collisions and background processes. Dominant sources of background are:

- synchrotron radiation,
- beam pipe remnant gas interaction (vacuum of ca. 10^{-9} hPa),
- stray protons, beam-halo,
- cosmic radiation and induced showers.

To suppress background, only events in a time window of 3ns around bunch crossing time t_0 are used for physics analysis. Two double scintillator veto walls upstream at $z = -6.5\,\text{m}$ and $z = -8.1\,\text{m}$ are used to identify out of time particles produced by the proton beam. Two time-of-flight (ToF) devices at $z = 7.9\,\text{m}$ and $z = -2\,\text{m}$ reject out of time events.

The H1 trigger system is separated into five levels, L1 - L5:

- **L1** needs $2.4\,\mu\text{s}$ (25 bunch crossings) to decide whether to keep the event. There are 128 L1 subtriggers, each of which is sufficient to fire an 'L1keep'-signal. Detector data has to be stored in pipelines during decision time.

- **L2** (since 1996) uses neural networks to classify event topologies. L2 starts the readout process.
- **L3** has not been operative during the acquisition of data considered in this analysis.
- **L4** is running on a processor-'farm' (parallel computer). A fast version of event reconstruction is performed, identifying energy clusters and tracks. Additionally, this level is used for online control of the detectors (calibration). The selected events are written to tape as raw data. This happens at a rate of 20 Hz.
- **L5** runs offline, performing full event reconstruction from raw data. Calibration and correction constants are applied and events are sorted into classes. Output is written in POT format (production output tape) and the more concise DST (data summary tape), starting point for physics analysis. Unclassified events are rejected and stored on special tapes.

Subtriggers 67 and 75

Subtriggers 67 and 75 are both used for the identification of electron candidates in the liquid argon. The setup of the individual subtriggers has been subject to various fluctuations over the years. Table 2.6 shows a typical composition of trigger elements. During datataking, various minor changes in thresholds and vetoing have occurred, but the basic conditions expressed by the trigger elements have remained the same:

- imposition of a lower limit to the energy in the e.m. calorimeter as well as an upper limit on the hadronic one
- no veto-wall proton related background timing
- at least one detected track candidate originating near the interaction point

Subtriggers 67 and 75 are roughly equivalent, except for minor changes in vetoing and application of thresholds. And indeed they do fire in conjunction most of the time. Still they have both been taken into account in order to optimize trigger efficiency (probability of firing of either subtrigger in case of a wanted event).

<table>
<tr><th>subtrigger</th><th>definition</th></tr>
<tr><td>67</td><td>LAr_el_1 && !BToF_BG && !VETO_inner && !VETO_outer && (zVtx_T0 || FwdRay_T0) || LAr_T0 && FToF_IA || !FToF_BG</td></tr>
<tr><td>75</td><td>LAr_el_2 && !BToF_BG && !VETO_inner && !VETO_outer && (zVtx_T0 || FwdRay_T0) && FToF_IA || !FToF_BG && (!RZ_non_vtx || RZ_sig1)</td></tr>
</table>

<table>
<tr><th colspan="2">trigger elements</th></tr>
<tr><td>LAr_el_1</td><td>BT above thresh 1 in em part and below in had</td></tr>
<tr><td>LAr_el_2</td><td>BT above thresh 2 in em part and below in had</td></tr>
<tr><td>BToF_BG</td><td>backward ToF hit background time window (p)</td></tr>
<tr><td>VETO_inner</td><td>Inner Veto Wall p rel. backgr. timing</td></tr>
<tr><td>VETO_outer</td><td>Outer Veto Wall p rel. backgr. timing</td></tr>
<tr><td>zVtx_T0</td><td>at least one ray</td></tr>
<tr><td>FwdRay_T0</td><td>any multiplicity, any topol in phi</td></tr>
<tr><td>LAr_T0</td><td>digital T0 (OR of TT exceeding analog thresh)</td></tr>
<tr><td>FToF_IA</td><td>forward ToF hit interaction time window (p)</td></tr>
<tr><td>FToF_BG</td><td>forward ToF hit background time window (!p&&!e)</td></tr>
<tr><td>RZ_non_vtx</td><td>upstream background (many non-vtx tracks)</td></tr>
<tr><td>RZ_sig_1</td><td>peak-significant pattern in z-vertex histogram</td></tr>
</table>

Table 2.6: *Typical settings of subtriggers 67 and 75.* `&&`, `||` *and* `!` *represent logical AND, OR and NOT respectively (see text for explanation on trigger elements)*

Chapter 3

Data and Software

3.1 Information Flow

3.1.1 Data Taking

A schematic representation of the flow of information during data taking is shown in figure 3.1. Detector readout is converted into digital signals stored in a pipeline during L1 decision time. The L4 filter farm performs preliminary reconstruction and writes raw data to tape. Each raw data file contains about 400 MB of data and about 60 raw data files fit onto one tape. Typically, a run under stable conditions lasts for a few hours, and a 400 MB file is filled, with a logging speed of about 1 MB/s, in 5 to 10 minutes. L5 offline reconstruction produces detailed POT (production output tape) and more concise DST (data summary tape) archives.

3.1.2 DST

The Data Summary Tape format written by L5 reduces the full detector output of an event to the size of a few kilobytes, depending on the number of tracks and clusters found. Detailed information, e.g. on individual hits in the trackers, is lost (but can be recovered from POT or RAW data), reconstructed tracks, clusters and physical variables (4-momenta, charges, x, y, Q^2) can be directly accessed together with an estimated error. Table 3.2 gives an overview of the amount of DST data processed. DST data is organized in *banks*, lists of a variable number of repetitions of fixed sets of entries (e.g. for each vertex-fitted track), the stored values being accessible to the user through keywords (fortran or C++ macros).

H1 software is almost exclusively coded in fortran 77. There is also some support of C++ [15] but this more modern language has probably arrived too late to play any significant rôle in H1. I have attempted the mixed approach of writing my own code in C++ while still accessing existing fortran libraries. After initial complications, this has resulted in pleasantly

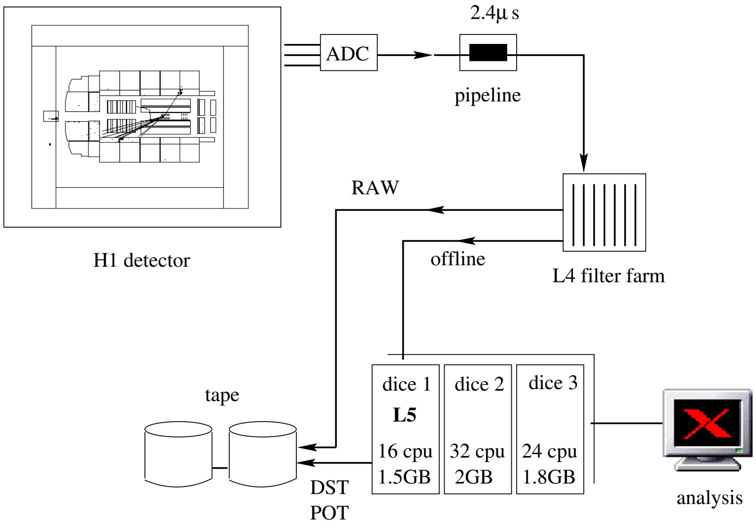

Figure 3.1: *Simplified diagrammatic view of data flow: Detector readout is stored in pipelines during trigger decision time, preprocessed by L4, RAW data directly written to tape, L5 running offline on the dice1 computer produces DST and POT, dice2 and dice3 are used to run batch jobs for physics analysis.*

readable, physics-oriented code.

3.2 Simulation and Reconstruction of Events

Reconstruction

The reconstruction process has the aim of recovering quantities useful for physical analysis from raw detector output. For track reconstruction, a first fit is performed from CJC hits only. These are the non-vertex-fitted tracks. From them, a vertex position is calculated. The average of this position over many events is taken into account by a second fit, yielding the vertex-fitted tracks. Calorimeter cluster reconstruction consists of two steps:

- For each readout channel, the ADC value is converted to the corresponding accumulated charge. This is achieved by means of a polynomial fit to the previously determined responses to known charges and correcting the result to account for LAr pollution.

- Cluster recognition: the cells corresponding to one incident particle are grouped. To reduce noise, only cells with energy depositions of more than 4 times the standard deviation of noise distribution are accepted as cluster centers, adjacent cells need to have more than 2 standard

year	bytes	events	int. lumi (tape)	int. lumi (used)
1994	60 G	5 M	$3.8\,\mathrm{pb}^{-1}$	$1.3\,\mathrm{pb}^{-1}$
1995	129 G	17 M	$6.1\,\mathrm{pb}^{-1}$	$3.9\,\mathrm{pb}^{-1}$
1996	232 G	22 M	$9.9\,\mathrm{pb}^{-1}$	$7.8\,\mathrm{pb}^{-1}$
1997	384 G	38 M	$28.2\,\mathrm{pb}^{-1}$	$23.2\,\mathrm{pb}^{-1}$
total	805 G	82 M	$48.0\,\mathrm{pb}^{-1}$	$36.3\,\mathrm{pb}^{-1}$

Figure 3.2: *DST quantity by year in bytes (1 G= 2^{30}), events and integrated luminosity. The right column gives the integrated luminosity that has been used for physics.*

deviations to be taken into account. A correction to the total cluster energy is applied to account for dead material losses.

.

Simulation

Great care has been taken to develop optimal simulation of the behaviour of all detector components. The program H1SIM (which is relying on GEANT [25]) has the primary task of simulating the showers, electromagnetic and hadronic, in the calorimeters. In order to stay within reasonable demands on computing power, two modes are available: A quick algorithm replacing the complex structure of detector materials by a homogenous medium is usually applied. In the case of a particle traversing a detector crack, the full cell geometry is taken into account.

Detector response is then calculated (ADC values). Finally, simulated electric noise is added and the output is handed to the reconstruction program just as if it were a real event.

Since the reversal of beam polarity in 1994, the electron tagger is not simulated anymore. Instead, there are H1 software library routines (`qpetac` and `acet44` for the taggers at 33 m and 44 m along the beam pipe) that for given run number and Bjorken y will return the probability for the scattered positron to end up in the tagger so that Monte-Carlo events can be weighted accordingly (see figure 5.1b).

3.3 Monte-Carlo

Monte-Carlo simulations have long become an essential part of experimental particle physics. Cross-sections are calculated by numerical integration of specific Feynman graphs. Random number generators are used to generate samples of simulated events.

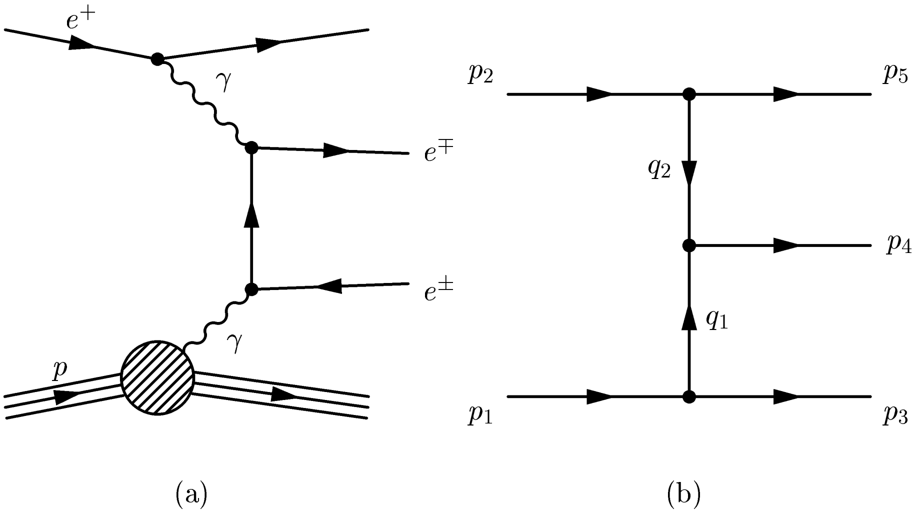

(a) (b)

Figure 3.3: *(a) Bethe-Heitler process with two γ in the t-channel, (b) kinematics as calculated by* LPAIR

3.3.1 LPAIR

The program LPAIR [16] is a Monte-Carlo generator for the simulation of lepton pair production in lepton-lepton, lepton-hadron or hadron-hadron interaction taking into account the multiperipheral graphs with two t-channel photons of figure 3.3a. This process is called after Bethe-Heitler[1]. Figure 3.3a represents two Feynman graphs, one each for the upper and the lower charge sign of the generated pair.

The main part of the cross-section of this process stems from regions of low t for both photons. Graphs with other topology are not included.

Kinematically, the process is treated as a $2 \to 3$ process as in figure 3.3b, independent of the particle content of the four-momenta p_3, p_4, p_5 (each may represent several particles). In the vertex $p_1 \to p_3$, elastic as well as inelastic interactions can be considered by the program.

3.3.2 LPAIR++

LPAIR++ is being developed by H.-C. Kästli with the purpose of including more graphs into the simulation of lepton pair production. In addition to the Bethe-Heitler graphs (figure 3.3a) calculated by LPAIR, the Compton-like graphs of figure 3.4 with both photons coupling to the scattered lepton (also called *Cabbibo-Parisi* graphs) are taken into account.

---

[1] Note that sometimes the same name is applied to the bremsstrahlung process mentioned in section 2.2.3, but for the remainder of this text, the name will be used exclusively in reference to the graphs in figure 3.3a.

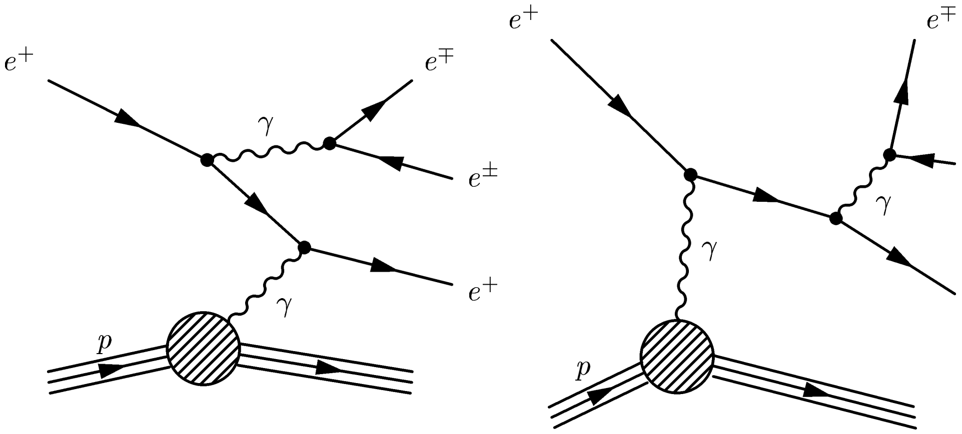

Figure 3.4: *Compton-like (Cabbibo-Parisi) graphs with two photons going off the incident positron line. These graphs (but not the crossed version where the two positrons in the final state swap positions) are calculated by* LPAIR++ *.*

As will become apparent, while the overall cross-section is not substantially affected by these graphs, the application of the cuts specific to this analysis will establish a notable difference between the output of the two generators.

Still not accounted for are the crossed graphs with the two positrons interchanged and the graphs with two photons going off the proton line (sometimes called after *Drell-Yan*) but their contribution is estimated to be small [18],[17]. Also, effects of graphs with a Z^0 taking the place of either γ are not going to be visible below an integrated luminosity of at least some $100\,\mathrm{pb}^{-1}$ [17].

3.3.3 DJANGO

DJANGO [19] simulates events of deep inealstic scattering (DIS). I have used it to determine the background to Bethe-Heitler lepton pair production due to decay of the scattered quark, resulting in final states indistinguishable from primary lepton production; background has turned out to be substantial, so that for this generator, reliability is as crucial as for the preceding ones.

DJANGO is in fact a front end to other programs: The Monte-Carlo geneator HERACLES produces events at the parton level which are then fragmented and hadronized using routines from LEPTO and JETSET. Graphs taken into account by DJANGO are represented in figure 3.5.

The involved quarks are assumed to be massless. For the simulation of heavy quark production (resonances), additional generators would be required.

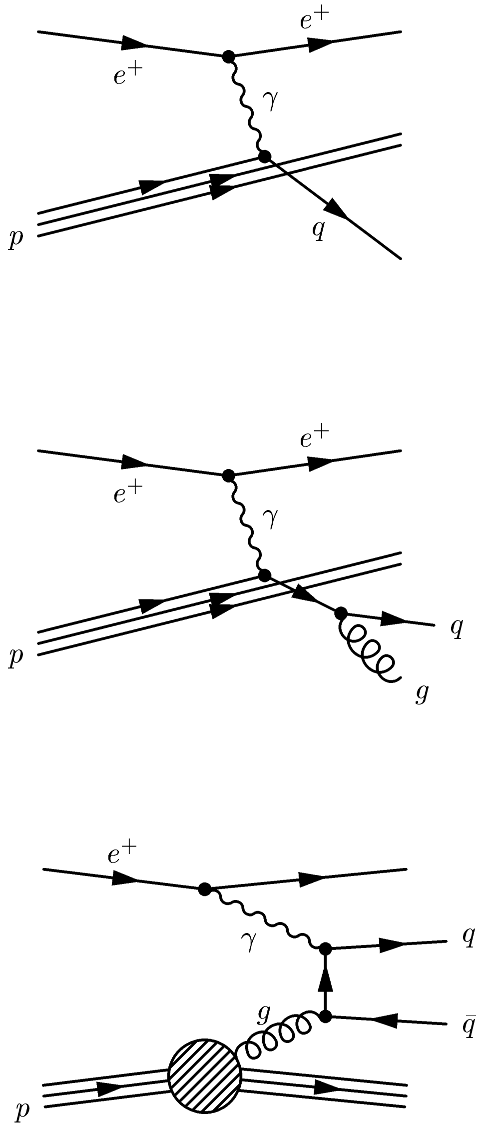

Figure 3.5: *Graphs calculated by* DJANGO *on the parton level to simulate* DIS*. The quarks considered massless.*

3.4 Electron Finders

3.4.1 XASELE

The electron finder XASELE [20] searches for electron-candidates in the liquid argon calorimeters by identifying sufficiently isolated energy depositions in the electromagnetic section that can be linked to a reconstructed track pointing towards it.

If more than one candidate is found, the program will fill a BOS-common structure with kinematic data and pointers to used tracks and energy clusters.

3.4.2 QESCAT

Designed to identify the scattered lepton, QESCAT does a good job in finding multiple leptons too. I have used it mainly to cover the SpaCal/BEMC region neglected by XASELE but also to provide a crosscheck of performance of the latter in the LAr calorimeter.

Both programs are standard H1 software and use H1PHAN [14] routines. Detailed methods and performance for electron identification are discussed in the next chapter.

Chapter 4

Analysis

4.1 Lepton Identification

All that is said in this chapter applies to electrons as well as to positrons. The terms electron and lepton will be used interchangeably for both (and no other lepton flavour) throughout. But see section 4.2.2 on charge determination and section 1.4.4 on muons. In this part of the analysis, I am drawing heavily from the theses by A. Schöning [20] and by P. Bruel [22].

In principle, the characteristics of a lepton in the detector are easily described. But in real life, dealing with a jumble of tracks and clusters, the balance between unjustified rejection and misidentification is rather delicate; especially pions are often hardly distinguishable from leptons at all.

Briefly, the strategy to identify leptons is the following: Find a reasonably concentrated energy cluster in the electromagnetic calorimeter. Check if the level of surrounding hadronic depositions is reasonably low. See if there is a track reconstructed from hits in the jet chamber that points more or less in the direction of your cluster.

Depending on how strictly these criteria are applied, more or less electrons will be found and more or less other particles (or tracks and clusters that match only coincidentally) will be misidentified as electrons.

Figure 4.1 shows a typical case of a lepton going into the forward region of the detector. Figure 4.2 features a more problematic case, this lepton has entered a ϕ-crack and its shower is not restricted to the e.m. section.

To establish cuts that will allow optimal lepton identification, I have used a sample of generated and reconstructed electrons evenly distributed in phase space (energies ranging from 10 to 50 GeV and flight directions covering the full solid angle). A similar sample where pions instead of electrons were simulated has served to determine a misidentification rate.

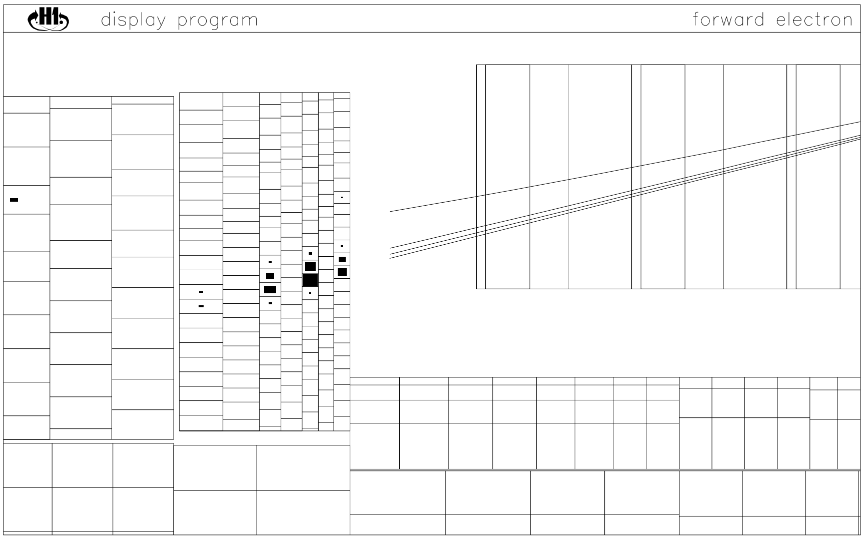

Figure 4.1: *close-up of an rz-view of the forward region, showing individual calorimeter cells: an electron is going through the forward tracker and ends up in the liquid argon, inducing a shower that is strictly confined to the electromagnetic section (the track elements are combined to more than one vertex-fitted track candidate).*

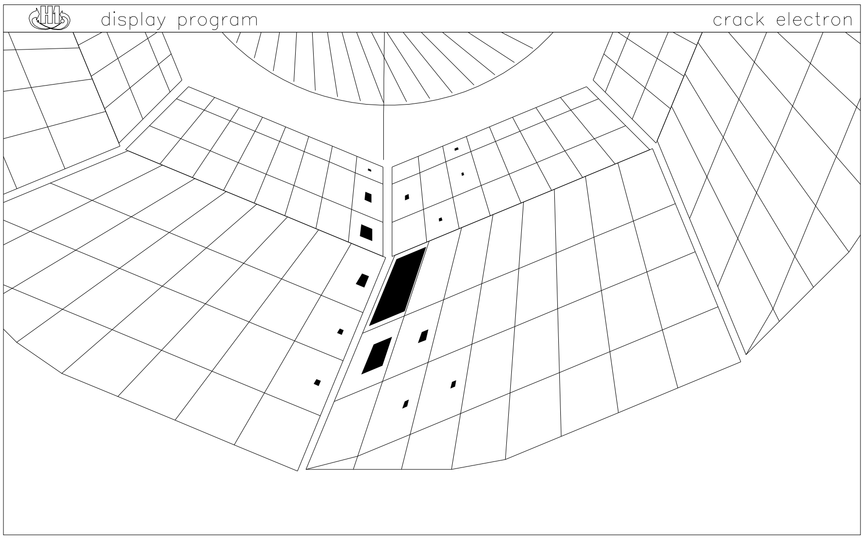

Figure 4.2: *close-up of an rϕ-view of the central liquid argon calorimeters, showing individual calorimeter cells: an electron is tracked by the central jet chamber and enters a LAr ϕ-crack. instead of depositing its energy in the electromagnetic calorimetersection, the hadronic section is directly reached, making identification of the particle as an e more difficult*

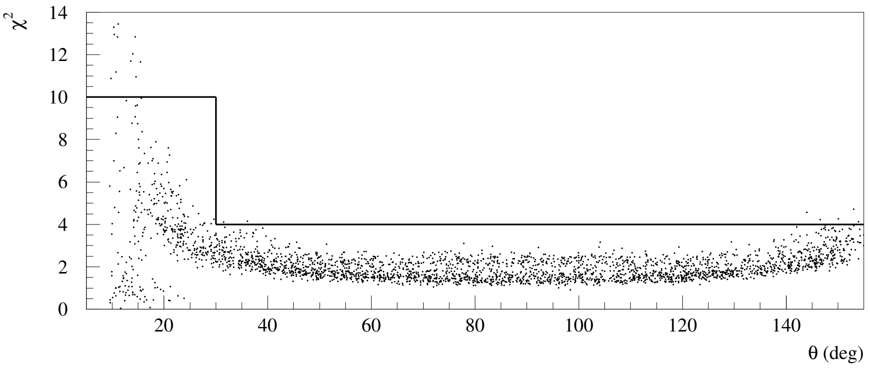

Figure 4.3: *χ^2/NDF of fitted tracks plotted against θ; the solid line indicates the applied cut. The limit of χ^2/NDF<4 has been loosened to 10 for $\theta < 30°$.*

4.1.1 Track Quality

Particle tracks are reconstructed from individual drift chamber hits. The quality of a reconstructed track depends on the number of hits linked. Figure 4.4 shows the number of tracker hits for found electrons.

The covariance matrix and corresponding χ^2 of the track fitted to the hits can be calculated (c.f. [21]):

$$V_{kl} = \mathsf{E}\left((x_k - \mathsf{E}(x_k))(x_l - \mathsf{E}(x_l))\right)$$

$$\chi^2 = \vec{x}^{\mathrm{T}} V^{-1} \vec{x}$$

where $\vec{x} = x_{1..n}$ are the positions of the fitted hits and E signifies the expectation value. The confidence level of a track is proportional to χ^2 divided by the number of degrees of freedom (NDF, the number of hits minus number of fitted parameters (five in our case of a fit to a helix)). Figure 4.3 shows the χ^2/NDF distribution of track fits for data and Monte-Carlo.

An additional criterium is the difference between track time and reconstructed interaction time. Out of time tracks have to be rejected as background. Figure 4.5a shows a comparison of data with Monte-Carlo for this time difference (absolute value taken).

4.1.2 Track-to-Cluster Distance

Figure 4.6 shows the distribution of $d_{\text{cl-tr}}$, the distance of the cluster center of mass to the extrapolated track. Due to the limited resolution of the forward tracker, a more scattered image emerges for small values of θ. To

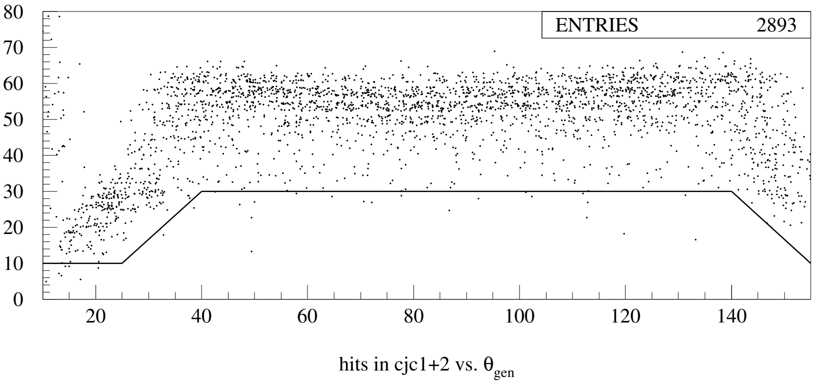

Figure 4.4: *Number of CJC hits of fitted tracks plotted against θ. The solid line indicates the minimal hit number required.*

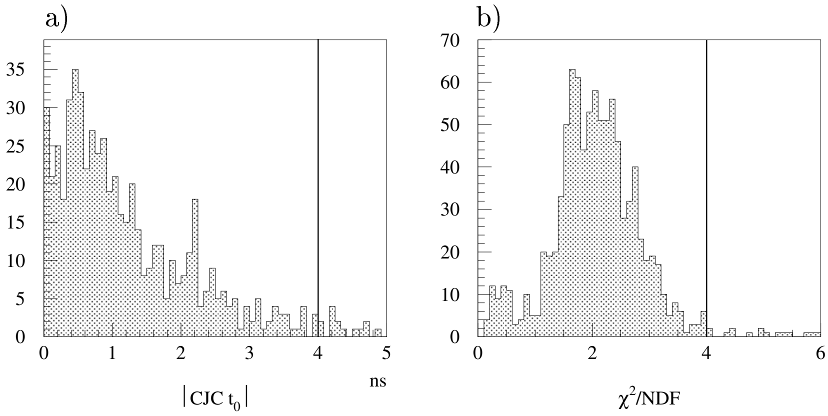

Figure 4.5: *(a) Absolute value of the difference between interaction time and CJC time. The solid line marks the maximal time difference tolerated (4 ns). (b) Distribution of track χ^2/NDF (central tracks), the line shows the maximal accepted value of 4.*

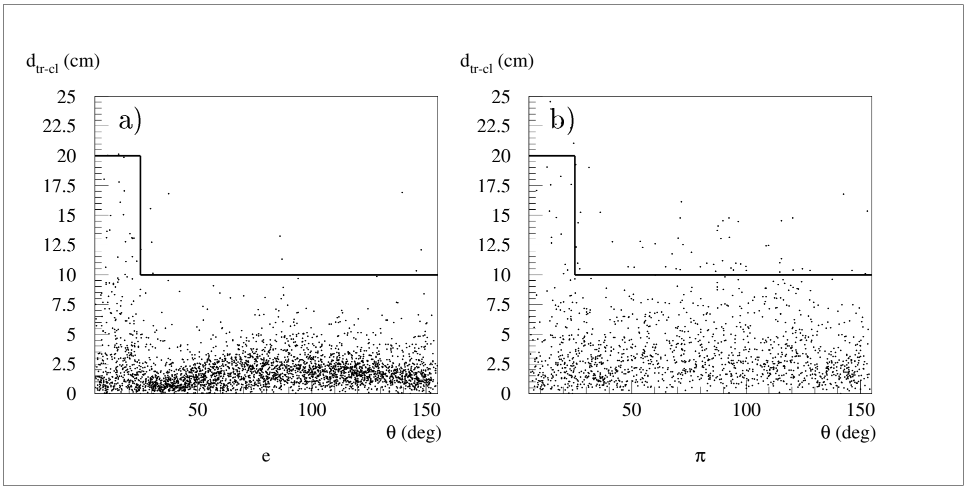

Figure 4.6: *Track-to-cluster distance $d_{tr\text{-}cl}$ determined for (a) electrons, (b) pions, plotted against θ. The solid lines show the maximal accepted values.*

reflect this, the tolerance of 10cm has been loosened to 20cm for values of θ below 25°.

4.1.3 Transverse Cluster Volume

Let $\vec{r}_i$ be the vectors pointing from the interaction vertex to the location of the cells belonging to the cluster, let

$$\vec{r} = \sum_i \vec{r}_i \frac{E_i}{E_{\text{cluster}}}$$

point to the cluster center of mass and take the corresponding unit vectors $\vec{e}_i$, $\vec{e}$. And let $\vec{a}_i = \vec{e}_i \times \vec{e}$, so that the norm of $\vec{a}_i$ is equal to the sine of the angle between cell i and the cluster center, $|\vec{a}_i| = \sin \angle(\vec{r}_i, \vec{r})$. Following reference [20], the transverse cluster volume is defined as

$$V_\perp = \sqrt{\left(\sum |\vec{a}_j|\right)^2 - \left(\sum \vec{a}_j\right)^2}$$

where the sums are over the cluster cells. This calculation is derived from reference [23] but is working with projections perpendicular to the particle direction. This has the advantage over an algorithm using longitudinal quantities that identification of leptons going into a detector crack, which often penetrate far inside the hadronic section, does not suffer significant loss in reliability.

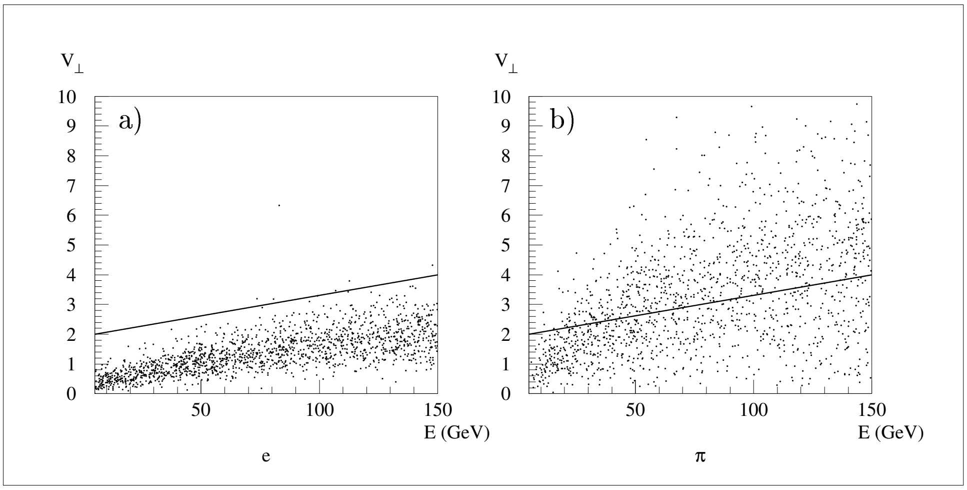

Figure 4.7: *Transverse cluster volume $V_\perp$ (see text) for (a) electrons, (b) pions, shown as a function of particle energy. The solid line marks the maximal accepted value.*

4.1.4 Cluster Isolation

To prevent us from misidentifying some cluster that is really part of a jet, an isolation criterium has to be applied. The straightforward procedure would be to look at the fraction of electromagnetic energy of the total cluster energy. Figure 4.8 shows the result of this: Many hadrons are effectively rejected, but for particles in the ϕ-cracks, no distinction between leptons and hadrons can be made. The cut as indicated in the picture with a 4° tolerance around the ϕ-cracks is maintained, but another criterium is required.

Two cylinders are cast along the vector pointing to the center of mass of the cluster in question, one with radius $r_\mathrm{i} = 10\mathrm{cm}$, the other with $r_\mathrm{o} = 25\mathrm{cm}$ (radii at calorimeter surface). Now, the ratios of the hadronic energy of the inner and outer cylinders each to the inner cylinder's energy,

$$R_\mathrm{i} = \frac{E_\mathrm{had}^\mathrm{inner}}{E^\mathrm{inner}}, \qquad R_\mathrm{o} = \frac{E_\mathrm{had}^\mathrm{outer}}{E^\mathrm{inner}},$$

are used to decide whether the cluster is sufficiently isolated. Figures 4.9 and 4.10 show the distribution of these quantities. The final cuts are set to $R_\mathrm{i} < 0.3$ and $R_\mathrm{o} < 0.02$.

A minimal energy of 5 GeV and a minimal transverse momentum of 1 GeV are required of the found electron. Table 4.1 shows a summary of the cuts used for lepton identification.

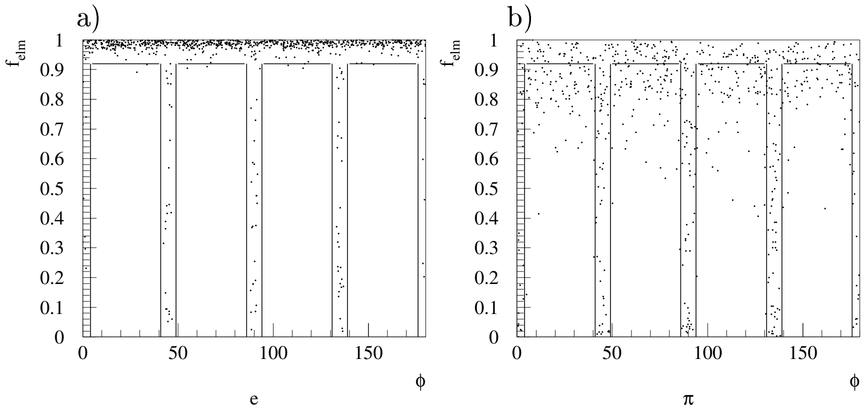

Figure 4.8: *Electromagnetic fraction of cluster energy vs.* ϕ *for (a) electrons, (b) pions. The LAr phi-cracks are clearly reflected by smaller values. The solid lines show the imposed cuts, a minimal fraction of* 92% *is required except for cluster centers closer than* 4° *to a* ϕ*-crack.*

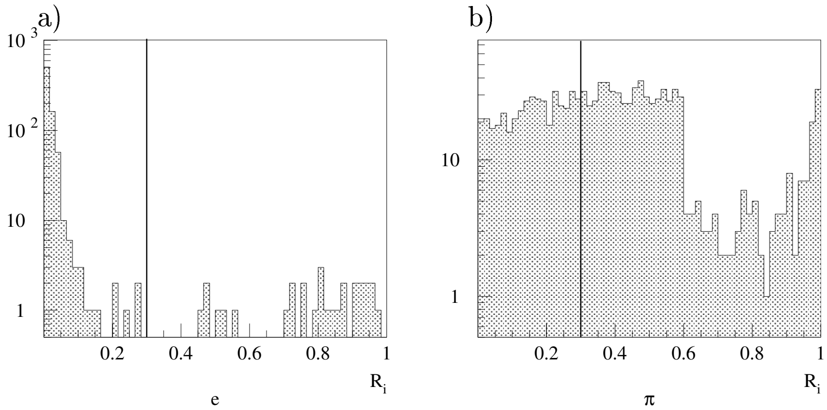

Figure 4.9: $R_{\rm i}$ *(hadronic energy along the track, see text) for (a) electrons and (b) pions. The solid lines indicate the maximal accepted value.*

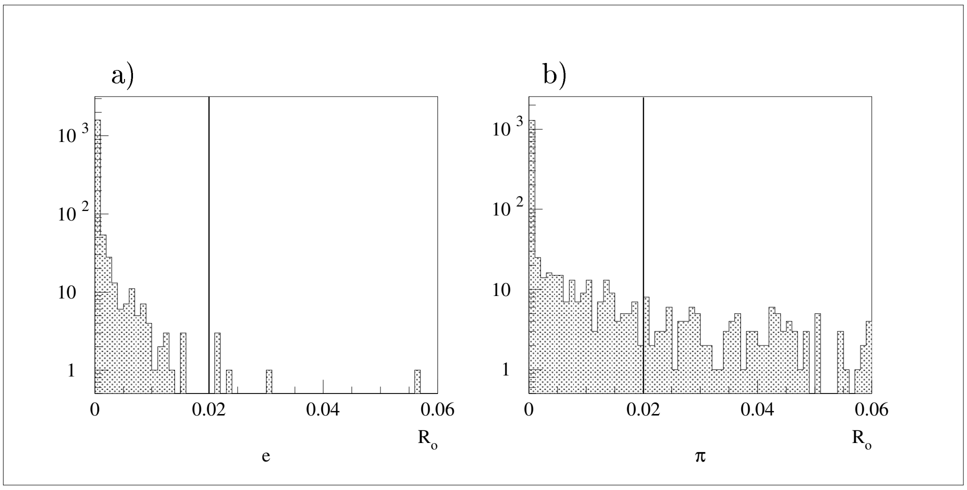

Figure 4.10: R_o *(cut on the hadronic energy in the vicinity of the track, see text) for (a) electrons and (b) pions. The solid lines indicate the maximal accepted value.*

electron finder criteria

- $p_\perp > 1\,\mathrm{GeV}$, $E > 5\,\mathrm{GeV}$
- culster-to-track distance $d_{\text{cl-tr}} \begin{cases} < 10\,\mathrm{cm} \\ < 20\,\mathrm{cm}\ \text{(forward)} \end{cases}$
- cluster transverse volume $V_\perp < 2 + E/75\,\mathrm{GeV}$
- number of tracker hits $\begin{cases} > 30\ \text{(center)} \\ > 10\ \text{(back/forward)} \end{cases}$
- track fit χ^2/NDF< 4 (forward: < 10)
- $|\mathrm{CJC}\,t_0| < 4\,\mathrm{ns}$
- e.m. energy fraction $f_{elm} > 92\%$ (non crack)
- cluster isolation: $R_\mathrm{i} < 0.3$, $R_\mathrm{o} < 0.02$

Table 4.1: *summary of criteria applied for electron identification*

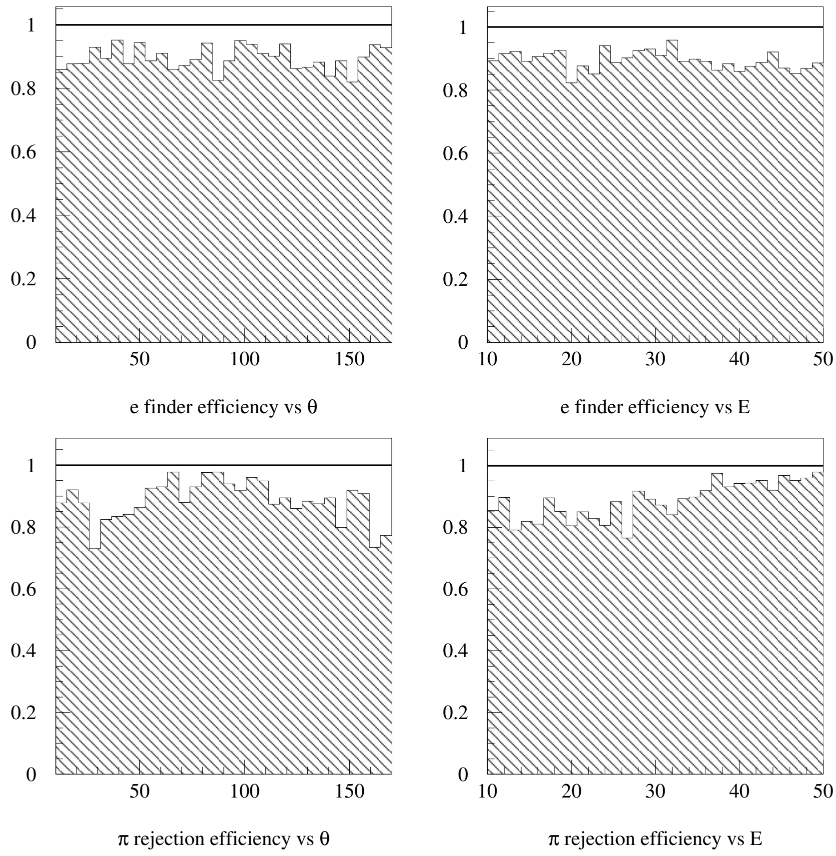

Figure 4.11: *efficiencies for e identification and π rejection as functions of θ and of particle energies*

4.1.5 Finder Efficiency

With the cuts set to the values decided upon in the previous section, an efficiency for the identification of a single electron of 90% is attained, θ-dependence is shown in figure 4.11. Pion rejection efficiency is also around 90% for the examined sample, but improves significantly with increasing particle energy.

Once an electron is identified, analysis quality still hinges on the precision of the reconstructed four-momentum. The plots of figure 4.12 show the errors of reconstructed energies and azimuthal angles of the found electrons. One sigma of energy reconstruction precision turns out to be 7% at an average $E_{\mathrm{rec}}/E_{\mathrm{gen}}$ of 96% while for θ, one sigma is about 0.5°.

In the plot of $E_{\mathrm{rec}}/E_{\mathrm{gen}}$ versus the z coordinate, the z cracks of the detector become clearly visible: Energy is lost in the cracks and the reconstructed value tends to be too low.

4.1.6 Exclusion of the BBE Region

The backward barrel electromagnetic calorimeter (BBE) poses an additional problem. There is no hadronic section covering this region, so no cuts on f_{elm}, R_{i} or R_{o} are practicable. Figure 4.13 shows the energy deposition of a particle going into the BBE. It is impossible to say from the shape of the cluster whether this was an electron or some other particle. As a consequence, going over the DST database, a lot of misidentified particles accumulate in the BBE region. Not much can be done about this except excluding the entire region. Thus, leptons with an azimutal angle of $138^\circ < \theta < 158^\circ$ are not taken into account for further analysis.

4.2 Event Selection

4.2.1 Preselection

Before deciding upon the application of stringent cuts, it is good policy to produce a file of events passing loosened cuts, that on one hand will safely contain all events of ultimate interest and on the other hand has a limited size so as to allow frequent processing for detailed analysis (going over the entire DST database takes of the order of one week). In particular, events should be selected regardless of triggers to have control over events lost later on due to trigger inefficiency.

In order to keep track of the total luminosity corresponding to the analysed sample, events rejected because some detector component had been inoperative (so-called HV (high voltage) reject) have to be removed from the beginning, i.e. at the time processing the full data sample. These rejects will simply result in a decreased overall luminosity and will not enter into later considerations. Table 4.2 lists the HV bits I have requested to be zero, corresponding to the related detector component being functional.

The cuts listed in table 4.3 have been imposed for event preselection: Two or more electrons are required, one of which must be in the LAr calorimeter (i.e., considering the BBE cut, $8^\circ < \theta < 138^\circ$) and both with an energy above 10 GeV. One electron must have a transverse momentum greater than 10 GeV, a second one needs a $p_\perp > 2\,\mathrm{GeV}$. The event needs to have a reconstructed vertex z coordinate of $|z_{\mathrm{vtx}}| < 35\,\mathrm{cm}$. A total of 3080 events are found to pass these preliminary cuts.

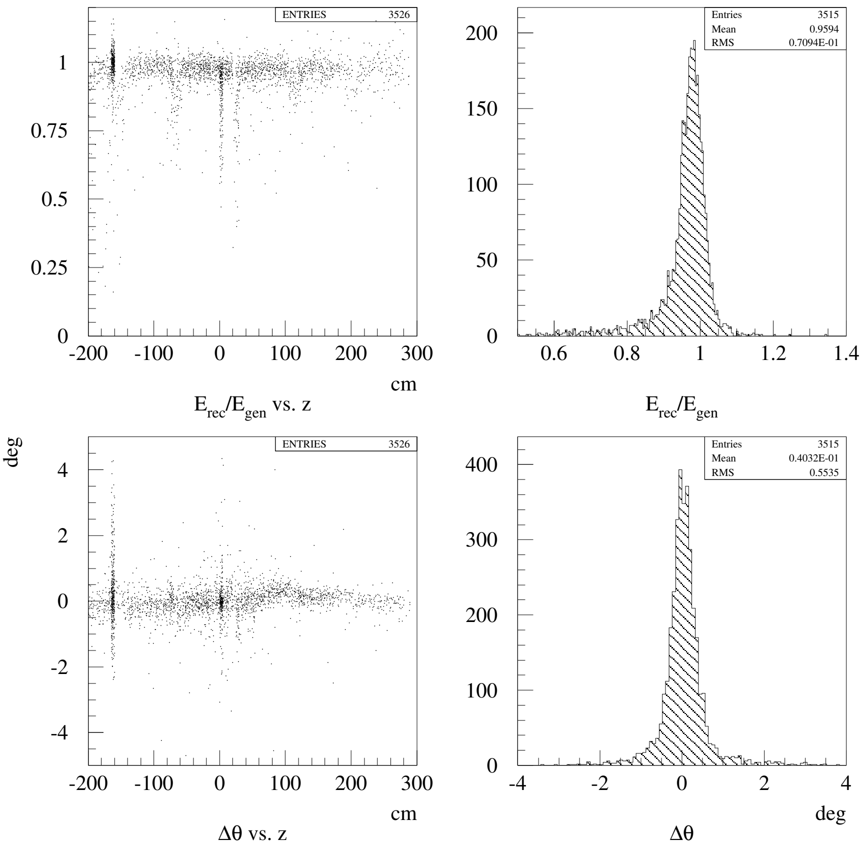

Figure 4.12: *Quality of reconstructed lepton properties: Comparison of reconstructed and generated energies and azimuthal angles,* E_{rec}/E_{gen} *and* $\Delta\theta = \theta_{rec} - \theta_{gen}$*, in the left plots shown as a function of z. The z cracks become clearly visible as a source of energy underestimation. the tested sample had electrons uniformly distributed in* θ*, resulting in an accumulation of entries at around* $z \approx -160\,cm$*, the SpaCal covering a large range of* θ *at constant z. Poorly reconstructed lepton energies at around this z-value indicate particles hitting the BBE (see section 4.1.6).*

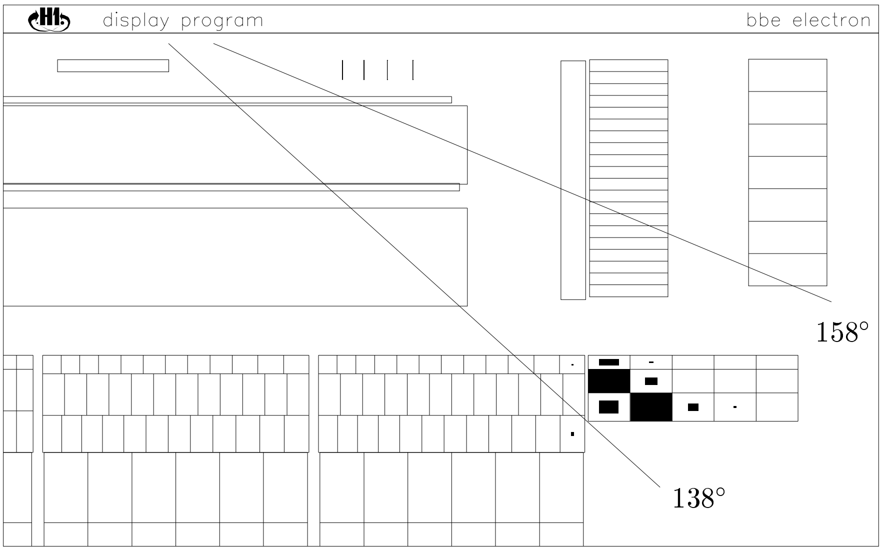

Figure 4.13: *BBE cut: This close-up of an rz-view of the detector shows a particle going into the BBE calorimeter, illustrating how the absence of a hadronic calorimeter section accounts for energy underestimation and precludes reliable identification. Approximate limits of the excluded range of* $138^\circ < \theta < 158^\circ$ *are shown.*

keyword	detector component
`BBL3CP`	Central Prop. Chambers, CIP/COP
`HVSTCPI`	Central Prop. Chamber, CIP
`HVSTCPO`	Central Prop. Chamber, COP
`BBL3VETO`	Veto Counters
`HVSTVETO`	Veto Counters
`ALL_CJ`	all CJC bits in all words
`ALL_CP`	all CP bits in all word
`HVSTBDC0`	Backward Drift Chamber
`HVSTBDC1`	Backward Drift Chamber
`BBL3SPAC`	Spacal bit in BBL3 word
`BBL3LAR`	Liquid Argon
`ALL_LAR`	all LAR bits in all words
`ALL_LUM`	all LUMI bits in all words

Table 4.2: *List of HV bits required zero. Keywords appear in bank HVST fed to subroutine HVBITS. An HV- (high-voltage-) bit is set in case of the corresponding detector component being inoperative.*

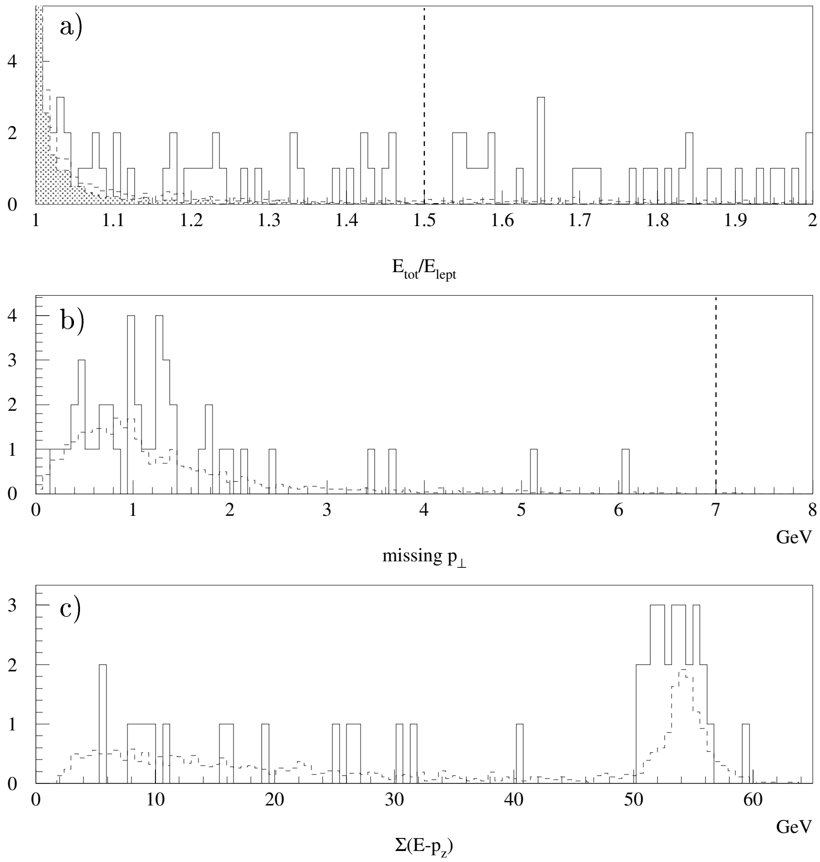

Figure 4.14: *plot of cut parameters (the dashed line represents* LPAIR++ *MC). (a) ratio of total energy deposited to the sum of energies of found leptons* E_{tot}/E_{lept}*, the elastic portion of MC expectation is shaded; (b) total transverse momentum ("missing* $p_\perp$*") after a cut of* $E_{tot}/E_{lept} < 1.4$*; (c) sum of* $E - p_z$ *of found tracks after additionally cutting on* $p_{\perp,tot} < 7$*; no further cut on this quantity was applied. Compare figures 4.15,4.21 for a distinction between elastic and inelastic events*

preselection cuts

- $z_{\mathrm{vtx}} < 35\,\mathrm{cm}$
- $\geq 2e$ in main detector, $\geq 1e$ in LAr
- $\theta_{1,2} \in [8^\circ \ldots 177^\circ] \backslash [138^\circ \ldots 158^\circ]$
- $E_{1,2} > 10\,\mathrm{GeV}$
- $p_{\mathrm{t}1} > 10\,\mathrm{GeV}; \quad p_{\mathrm{t}2} > 2\,\mathrm{GeV}$

Table 4.3: *Summary of cuts for event preselection. Identification of a third lepton is restricted by the cuts for e identification* ($p_\perp > 1\,\mathrm{GeV}, E > 5\,\mathrm{GeV}$, *see table 4.1).*

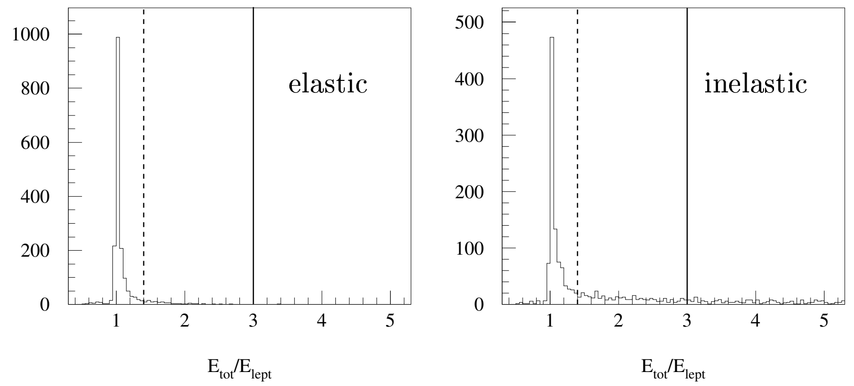

Figure 4.15: *The quantity* E_{tot}/E_{lept} *shown separately for elastic and for inelastic events. The dashed line shows the cut value of 1.4, loosened to 3 (solid line) in figure 5.1. Both elastic and inelastic events peak well inside these cuts, but still a substantial fraction of inelastic events is lost (c.f. table 5.2)*

4.2.2 Final Cuts

Cut on hadronic Energy

Even after the isolation cuts of the electron finders, there are still a lot of jet constituents misidentified as electrons. If we were only looking for elastic events, a rigorous cut on the total energy in the detector apart from the identified electrons would help. Yet we are not in principle bent on exclusion of jets, even if we are not interested in their specific properties. Fortunately – strictly speaking in the present context – as the Monte-Carlo sample of inelastic events shows, most jets leave the detector through the beam pipe with only a few showers remaining in the surrounding calorimeter volume. So even if a cut on hadronic energy will noticeably reduce the fraction of identified inelastic events, this effect is not be dramatic.

A straightforward approach would be to cut on $E_{\text{tot}} - E_{\text{lept}}$, the total energy minus the energies of the found leptons. However, for higher lepton pair masses, we might want to allow for a higher threshold to account for noise or cells not included into the cluster by mistake. A cut on $E_{\text{tot}}/E_{\text{lept}}$ yields satisfactory results, but still, the background level increases for high energies. This circumstance holds the temptation to further suppress hadronic energy by inclusion of an exponent α into the expression to effect a cut of the form

$$\frac{E_{\text{tot}}}{E_{\text{lept}}^{\alpha}} < \beta,$$

which indeed works well but also tends to suppress perfectly sound events at very high masses, which are exactly what this analysis is about, so this option has not been pursued and the cut is set to $E_{\text{tot}}/E_{\text{lept}} < 1.4$. In figure 4.15, the effect of this cut is illustrated for elastic and for inelastic LPAIR++ data separately.

Cut on missing $p_{\perp}$

The initial state, two colliding beam particles, has no momentum transverse to the beam line. All transverse momentum detected in the final state is therefore either due to calibration uncertainties or to particles that escaped detection, notably neutrinos. Especially if only two leptons are found, to infer the existence of a third one lost in the beam pipe is only tenable if "missing" transverse momentum is low. The cut is not sensitive but serves to exclude a few far out candidates; it is set to $p_{\perp} < 7\,\text{GeV}$.

$\sum(E - p_z)$

No cut on $\sum(E-p_z)$ is applied, but comparison of this quantity's distribution with LPAIR++ (figure 4.16) after imposition of all other cuts shows that the remaining samples are similar. The initial state value of this quantity is

final cuts
• $|z_{\rm vtx}| < 35\,\rm cm$ • $\geq 2e$ in main detector, $\geq 1e$ in LAr • $\theta_{1,2} \in [8^\circ \ldots 177^\circ] \backslash [138^\circ \ldots 158^\circ]$ • $E_{1,2} > 10\,\rm GeV$ • $p_{\perp 1} > 10\,\rm GeV; \quad p_{\perp 2} > 5\,\rm GeV$ • $p_\perp^{\rm missing} < 7\,\rm GeV$ • $\frac{E_{\rm total}}{E_{\rm leptons}} < 1.4$

Table 4.4: *Summary of cuts for final event selection; identification of a possible third e is conditioned by the e-finder criteria* ($p_\perp > 1\,\rm GeV, E > 5\,\rm GeV$, *see table 4.1)*

twice the lepton beam energy (some 55 GeV), reconstructed values below this are indicative of particles lost in backward direction.

Charge Determination

Figure 4.19 illustrates charge reconstruction efficiency. In spite of the rather good value around 90%, no cut was imposed on lepton charge. Any cut on reconstructed charge (say, requiring an e^-) would cost us a substantial fraction of wanted events – even if charge reconstruction were flawless – because if only two leptons are visible, they will have the same charge half of the time.

Multiple Identification

It can happen in principle that a single electron is reconstructed to two particles, especially in case of an inelastic event where the program can become confused by the large number of track candidates. This effect can be efficiently suppressed by excluding a solid angle of $4^\circ \times 4^\circ$ around any found electron from the search for further electrons. Simulation shows the chances that two electrons are in fact present that close to one another to be very small. And even in this unlikely case, the small angle between the electrons will result in a low m_{ee}, so that these events are irrelevant to the invariant mass spectrum.

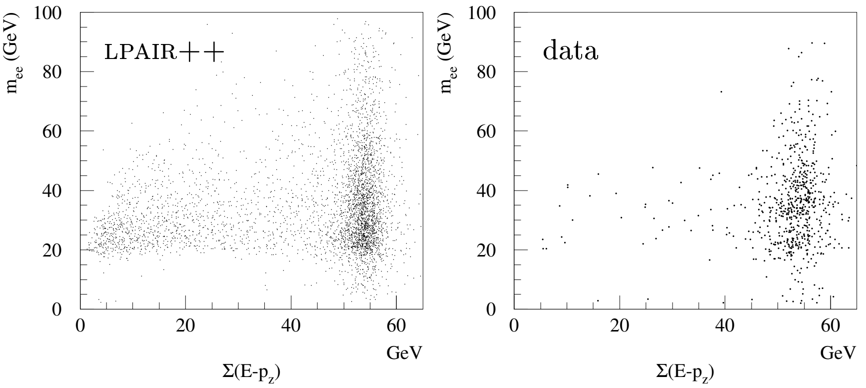

Figure 4.16: $\sum E - p_z$ *vs.* m_{ee} *of* LPAIR++ *Monte-Carlo (left) and data (right) after imposition of all cuts. One data point corresponds to the luminosity of 46 MC points.*

The cuts as finally imposed are summarized in table 4.4. The most sensitive of these are on $p_\perp$ and on $E_{\mathrm{tot}}/E_{\mathrm{lept}}$, their behaviour is illustrated in figures 4.17 and 4.18.

4.2.3 Rejected Events

The discussed cuts efficiently reduce background, but also a significant fraction of wanted data is lost. This number must be determined for the calculation of the cross-section (see next chapter), but also for mere comparison with Monte-Carlo, it is interesting to check whether this loss is at least equally distributed over event kinematics, or if some regions are severely disadvantaged. For Monte-Carlo, figure 4.21 compares events preselected and events surviving all cuts, showing the distributions of Q^2 and pair mass for elastic and inelastic events separately. The region of $Q^2 \approx 200\,\mathrm{GeV}^2$ is entirely suppressed because of the BBE cut (preselected events of this class are shown in the Q^2 plot, but not in the m_{ee} plot). Due to the cut on hadronic energy, a significantly greater fraction of inelastic events is lost, even up to 50%, but for high m_{ee} this becomes less dramatic. A proper estimation of overall acceptance is given in the next chapter.

Events passing the preselection (table 4.3) but not the final cuts (table 4.4) are plotted in figure 4.20. They are expected to consist of DIS background to more than 90%. The good agreement with data reassuringly confirms that background simulation was realistic.

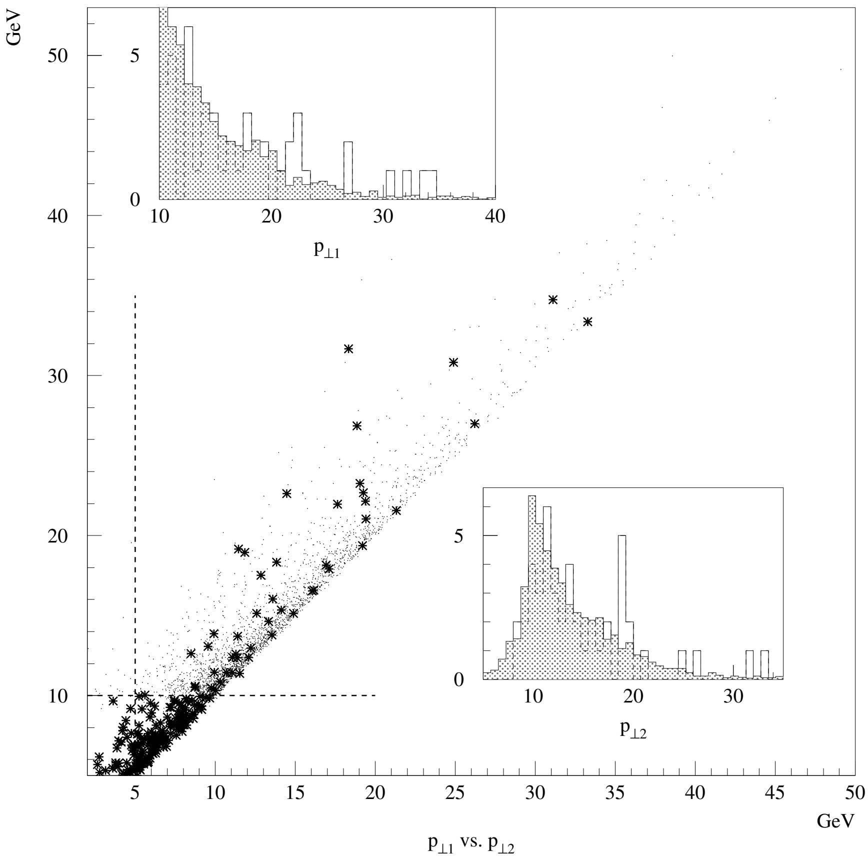

Figure 4.17: *Distribution of the transverse momenta of the found lepton pair, $p_{\perp 1} > p_{\perp 2}$. Asterisks are data points, small dots show Monte-Carlo distribution (where 46 MC events correspond to the luminosity of a single data point). The two dashed lines indicate the final cuts on $p_\perp$. The two insets show $p_\perp$-distribution after these cuts, data appears in the blank plot, MC is the shaded region. In case of three found e, the two largest $p_\perp$ are considered. Events with a large difference $|p_{\perp 1} - p_{\perp 2}|$ tend to have a third found e to keep the missing $p_\perp$ below the cut value of* 7 GeV.

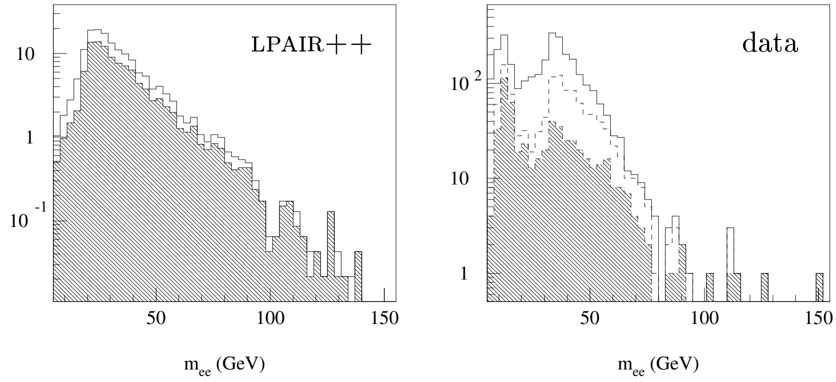

Figure 4.18: *Effect of the cut* $E_{\rm tot}/E_{\rm lept} < 1.4$ *on Monte-Carlo (left) and data (right). The blank plot is of preselected events. For data, an intermediate cut of* $E_{\rm tot}/E_{\rm lept} < 3$ *is shown (dashed histogram).*

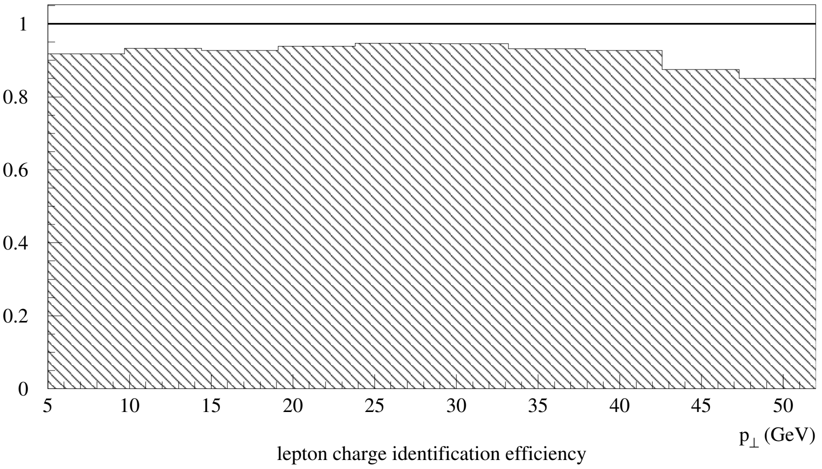

Figure 4.19: *Charge determination efficiency of leptons generated evenly distributed in energy and solid angle, as a function of* $p_\perp$*; there is a maximum at around* 30 GeV*, for smaller values, the particles travel through a smaller portion of the CJC, resulting in a less reliable fit on track curvature, for large values of* $p_\perp$ *(and therefore of* E*), curvature becomes smaller and is more often misidentified.*

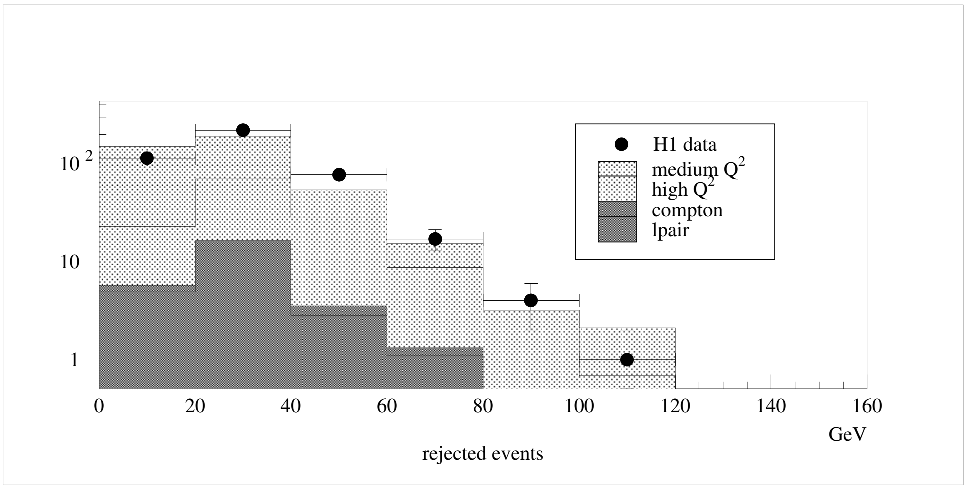

Figure 4.20: *Events preselected but rejected by the final cuts plotted against the electron-pair invariant mass m_{ee}. The dark shaded region is* LPAIR++ *MC, the light shaded region is* DJANGO *background, black dots are data points (c.f. figure 5.2). Some* 95% *of rejected events are background. (only statistical errors are represented by the error-bars)*

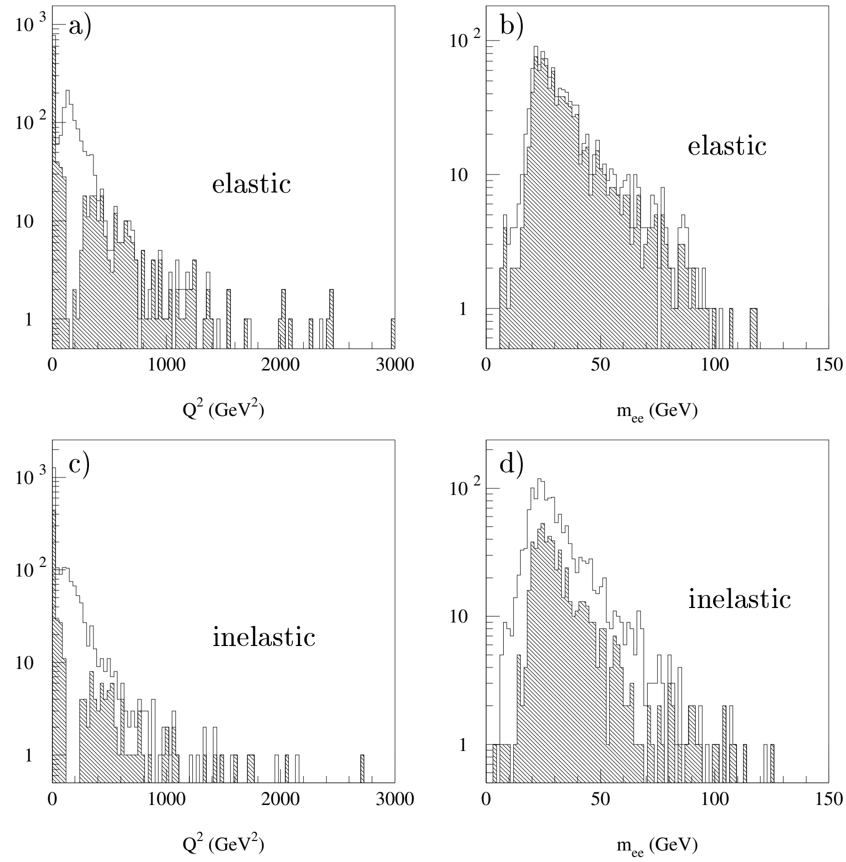

Figure 4.21: *Monte-Carlo events passing preselection (blank) and final cuts (shaded). A greater fraction of inelastic events is lost as a consequence of the cut on hadronic energy. The region of* $Q^2 \approx 200\,\mathrm{GeV}^2$ *is suppressed as a consequence of the BBE cut (section 4.1.6). Events lost to the BBE cut are not shown as preselected in the plots of* m_{ee}*. In total,* 66% *of preselected events pass the final cuts (c.f. table 5.2).*

Chapter 5

Results

5.1 Comparison with Expectation

Selected data is compared with a collection of Monte-Carlo samples as follows:

- **lepton pair production**: $8^\circ < \theta < 177^\circ$, $E > 10\,\mathrm{GeV}$ for two $e^\mp$ with one's transversal momentum $p_\perp > 10\,\mathrm{GeV}$ and the other one's $p_\perp > 2\,\mathrm{GeV}$.
  - LPAIR: 2.34 pb (1.19 pb inelastic + 1.15 pb elastic) with a luminosity of 2092 per pb (factor of 57.6 compared to data)
  - LPAIR++ : 2.77 pb (1.48 pb inelastic + 1.29 pb elastic), luminosity 1684 per pb (factor 46.4)

  Note that, with these cuts, inclusion of Compton graphs (LPAIR++) makes a difference in cross-section of 18%, for inelastic scattering even 24%. This effect is expected to decrease slightly with the inclusion of crossed graphs.

- **DIS background**: DJANGO 6.2
  - $Q^2 > 1000\,\mathrm{GeV}^2$: 245 pb with a lumi of 293 per pb (factor 8.1)
  - $1000\,\mathrm{GeV}^2 > Q^2 > 90\,\mathrm{GeV}^2$: some 6300 pb with a lumi of 76 per pb (factor 2.1) Only a small fraction of these events will be selected.

Table 5.1 gives an overview over examined data samples.

5.1.1 3e found

In the case of three identified leptons, there are of course three possibilities for the formation of a pair's invariant mass. The method I have adopted is

origin	lumi	x-section
H1 data 1994-1997	$36.3\,\mathrm{pb}^{-1}$	
LPAIR	$2092\,\mathrm{pb}^{-1}$	$2.34\,\mathrm{pb}$
LPAIR++	$3367\,\mathrm{pb}^{-1}$	$2.77\,\mathrm{pb}$
DJANGO high Q^2	$293\,\mathrm{pb}^{-1}$	$245\,\mathrm{pb}$
DJANGO medium Q^2	$76\,\mathrm{pb}^{-1}$	$6323\,\mathrm{pb}$

Table 5.1: *Examined data samples: The* LPAIR *and* LPAIR++ *files were generated according to the preselection cuts (table 4.3), the high- and medium-*Q^2 DJANGO *samples have* $Q^2 > 1000\,\mathrm{GeV}^2$ *and* $1000\,\mathrm{GeV}^2 > Q^2 > 90\,\mathrm{GeV}^2$ *respectively.*

simply choosing the two particles with the smallest value of θ, i.e. furthest deflected from electron beam direction. Another interesting quantity is m_{123}, the mass of all three particles, listed in the appendix for the eight events of figure 5.1a.

Figure 5.1 shows the events where three electrons have been detected. Background is much more suppressed compared to events with only two detected electrons. This has allowed me to loosen the cut on hadronic energy to $E_{\mathrm{tot}}/E_{\mathrm{lept}} < 3$. All other cuts were left unchanged. Statistics is still very poor, eight events have been selected. They are represented indivitually in the appendix.

The case of one electron detected in the tagger is represented in a separate plot; 7 events fall into this category. No DIS background at all is simulated here, because already for values of Q^2 above some $4\,\mathrm{GeV}^2$, the scattered lepton is deflected out of the beam pipe and will consequently not reach the tagger. Examination of MC data shows that chances for a member of the generated pair to end up in the tagger are neglegible.

As described in section 3.2, there is no simulation for the electron tagger. Monte-Carlo events have been weighted according to `qpetac` and `acet44`. The result of this is not in agreement with observation, possibly due to photoproduction background. In later plots, tagged electrons will be ignored, i.e. the events shown in figure 5.1b will be treated together with regular $2e$-events.

5.1.2 2e found

Statistics for events with two detected electrons is more reasonable, at a cost of higher background. Figure 5.2a shows events with two found electrons only, on a logarithmic scale. In 5.2b (with a magnified view of the highest four bins in 5.2c), all events selected by the cuts in table 4.4 are included: $2e$-events as well as $3e$-events, but contrary to figure 5.1, the cut on $E_{\mathrm{tot}}/E_{\mathrm{lept}} < 1.4$ is maintained for all events. The resulting sample (36 events) is what I

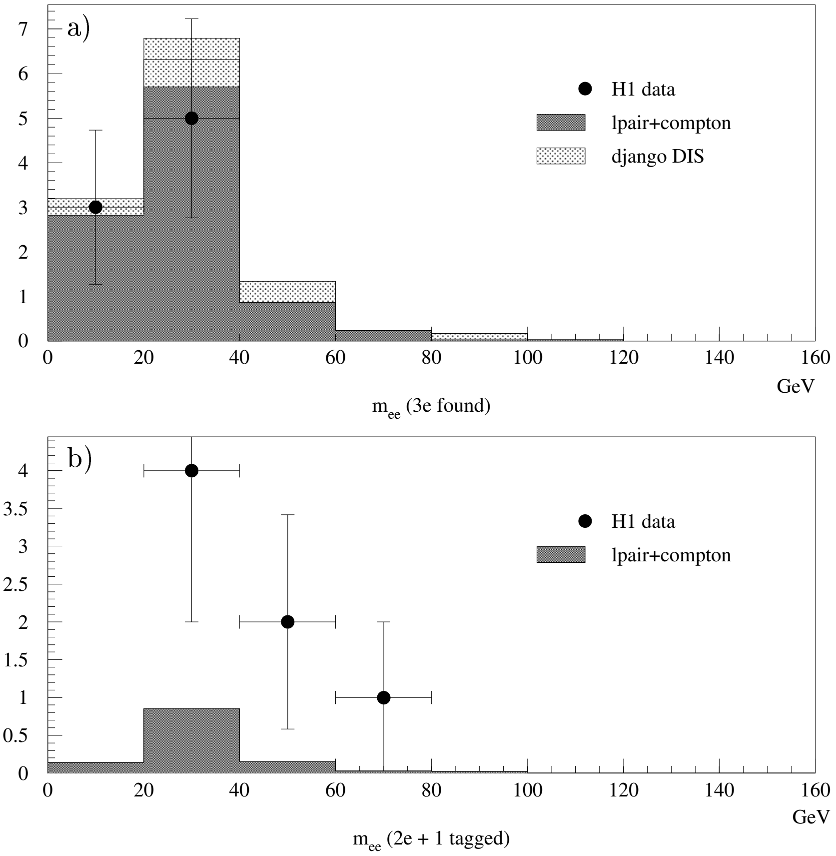

Figure 5.1: *Selected events with three detected electrons. The dark shaded region is Monte-Carlo data for Bethe-Heitler plus Compton, the light shaded region for DIS background. The upper plot shows events with 3 electrons in the main detector, events in the lower plot have one tagged electron. See text on tagger simulation. Note that as background is much suppressed for 3e-events, the cut on hadronic energy has been loosened to* $E_{tot}/E_{lept} < 3$ *for this plot. To allow direct comparison with figure 5.2, a pair mass* (m_{12}, *see text) is plotted. See the appendix for the total invariant mass* m_{123}.

am going to calculate the cross-section from. The four events with $m_{ee} > 80\,\mathrm{GeV}$ shown in the magnified view 5.2c are individually represented in the appendix.

Note that the event with highest m_{ee} is well inside the top bin ($m_{ee} = 150\,\mathrm{GeV}$) where there is no MC expectation at all. Thus it may be justified to talk of a small excess in the highest one or two bins – even this single event was very unlikely to occur, if it is not of DIS origin (see the appendix for a detector picture), an upper limit of its probability is some 2% – but for the cross-section, this is compensated for by the insufficient number of events found for $80\,\mathrm{GeV} < m_{ee} < 100\,\mathrm{GeV}$, and of course, much more statistics would be required to make a statement with any conviction.

5.2 Acceptance

To estimate a value for overall acceptance, I rely on comparison with Monte-Carlo data. Through several analysis steps, the number of surviving events is monitored :

- **trigger efficiency** $\varepsilon_{\mathrm{trig}}$: probability of either subtrigger (67 or 75) firing in case of a wanted event.
- **pair identification efficiency** ε_{ee}: probability of identification of a lepton pair fulfilling the kinematical cuts
- **CJC time efficiency** ε_{t_0}: Fraction of events inside CJC time limits. With $\varepsilon_{t_0} = 98\%$, this cut is not sensitive.
- **acceptance of final cuts** $\varepsilon_{\mathrm{cuts}}$: fraction of events surviving the final cuts (table 4.4).

The ratio of surviving to initially generated events $\varepsilon = \varepsilon_{\mathrm{trig}}\varepsilon_{ee}\varepsilon_{t_0}\varepsilon_{\mathrm{cuts}} = 51\%$ is the acceptance (see table 5.2).

5.3 Background Separation

The cross-section of two-photon processes exclusively is to be determined, so we need to rely on Monte-Carlo to estimate what fraction $f_{ee}^{\gamma\gamma}$ of events in our final sample is of this origin. I find

$$f_{ee}^{\gamma\gamma} = 60\%.$$

A background rate of 40% is somewhat unsatisfactory but further reduction is only feasible at the price of even lower statistics and would not result in a smaller uncertainty in cross-section.

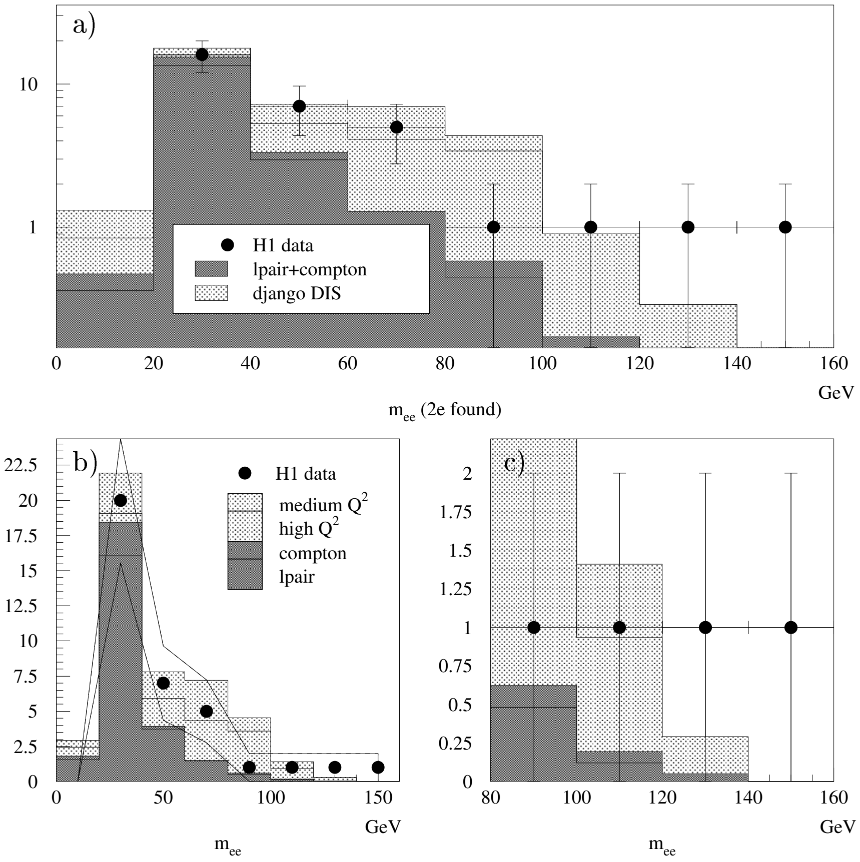

Figure 5.2: *(a) Events with two detected e; (b) Events with ≥ 2 detected e; (c) Magnified view of 4 highest bins of (b). The dark shaded region is* LPAIR++ *MC, the light shaded region is* DJANGO *MC, black dots are data points.*

	elastic	inelastic	total
total # of events	1249	1691	2940
triggered ($\varepsilon_{\text{trig}}$)	1079 (86%)	1461 (86%)	2540 (86%)
e pair found (ε_{ee})	1012 (94%)	1265 (80%)	2277 (90%)
CJC t_0 ok (ε_{t_0})	997 (98%)	1248 (98%)	2245 (98%)
all cuts passed ($\varepsilon_{\text{cuts}}$)	906 (91%)	583 (47%)	1489 (66%)
acceptance ε	73%	34%	**51%**

Table 5.2: *Acceptance is determined by looking at the fraction of generated MC events surviving the sequence of analysis steps: listed for elastic and inelastic events seperately is the total number and the fraction of survivors for triggering, ee-pair identification, CJC time and imposition of the ensemble of final cuts. The overall acceptance is determined to* 51%*.*

5.4 Systematic Errors

The following sources of systematic error are considered:

- **event reconstruction**: I have repeated the entire analysis with all cuts both loosened/tightened by one sigma. The difference in identified Monte-Carlo events is $+10\%/-15\%$. This is taken as the systematic error to account for migration effects.
- **background separation**: Also determined from Monte-Carlo data, this error was estimated by loosening the cuts on LPAIR++ and tightening them on background, then vice versa. The resulting uncertainty is $+13\%/-16\%$.
- **integrated luminosity**: The systematic error is taken from [27],[28] as 2%. This tends to be on the safe side, as the luminosity of later data-taking periods have been subjected to fewer corrections due to detector HV failures.
- **trigger efficiency**: In reference [28], a similar event toplogy is triggered. Their error on trigger efficiency of 8% is assumed.

Quadratic summation of these contributions yields a systematic error of $+18\%/-23\%$. Table 5.3 gives a summary.

5.5 Cross-Section

H1 1994-1997 data, corresponding to an integrated luminosity of $L = 36.3\,\text{pb}^{-1}$ has been searched for events with at least 2 $e^{\mp}$ with energies $E_{1,2} > 10\text{GeV}$

event reconstruction	+10% −15%
background separation	+13% −16%
luminosity	±2%
trigger efficiency	±8%
total	+18% −23%

Table 5.3: *overview of systematic errors by origin*

and transverse momenta $p_{\perp 1} > 10\text{GeV}$, $p_{\perp 2} > 5\text{GeV}$ in the angular region $\theta_{1,2} \in [8^\circ \ldots 177^\circ] \backslash [138^\circ \ldots 158^\circ]$. $N = 36$ events pass all cuts and the cross-section is calculated to

$$\sigma^{\text{vis}}_{ep\to eeeX} = \frac{N \cdot f^{\gamma\gamma}_{ee}}{\varepsilon \cdot L} = \frac{36 \cdot 60\%}{51\% \cdot 36.3\,\text{pb}^{-1}} = \left(1.17 \pm 0.19^{+0.21}_{-0.27}\right)\ \text{pb}$$

where the first uncertainty accounts for statistical, the second for systematic errors. The expectation from LPAIR++ Monte-Carlo data is

$$\sigma^{\text{vis, MC}}_{ep\to eeeX} = 1.47\,\text{pb}.$$

The two values are compatible within error bounds. The measured cross-section is *lower* than the expected one, so that we can confidently say that no excess whatsoever has been found.

Chapter 6

Conclusion

6.1 Summary

H1 1994-1997 data, corresponding to an integrated luminosity of $36.3\,\mathrm{pb}^{-1}$ has been searched for events with at least 2 $e^{\mp}$ with energies $E_{1,2} > 10\mathrm{GeV}$ and transverse momenta $p_{\perp 1} > 10\,\mathrm{GeV}, p_{\perp 2} > 5\,\mathrm{GeV}$ with $\theta_1 \in [8^\circ \ldots 138^\circ]$, $\theta_2 \in [8^\circ \ldots 177^\circ] \backslash [138^\circ \ldots 158^\circ]$. 36 events are found to pass all cuts and the cross-section is calculated to be

$$\sigma^{\mathrm{vis}}_{ep \to eeeX} = \left(1.17 \pm 0.19^{+0.21}_{-0.27}\right)\ \mathrm{pb}$$

which is *lower* than the Monte-Carlo expectation of 1.47 pb, but still within bounds of uncertainty.

6.2 Acknowledgments

I am grateful to Professor Eichler for providing me with a thesis subject that I found both technically and scientifically fascinating. He was always able to ask the right questions when I was in danger of getting swamped by technicalities and I have very much appreciated the friendly atmosphere he knows to create in his group. I am also grateful for the opportunity to visit DESY and present my results at the BSM meeting, where I had the pleasure of an enlightening, if late in schedule, discussion with Dirk Hoffmann.

My thanks go to the members of the Zürich group for their hospitality, their kind patience and their valuable advice; I have profited particularly from the experience of Christoph Grab, Urs Langenegger, Hubert Niggli and Stefano Passaggio.

Most of all, I want to thank Hadi Kästli, who has gone far out of his way to help me and whose kindness has added much to make these past 4 months as enjoyable as they have been to me.

The main physics-related benefit I have drawn from this work is the drastic first hand experience of the power of the Standard Model. Theory (in its manifestation as Monte-Carlo generators) has predicted I would find some 30 to 60 events among the 82 million collected on DST, and, miraculously, 36 I did find. My epistemological misgivings against particle physics have been much appeased and I do believe that valuable insight into the *nature of things* is still to be gained from this branch of science.

*

Appendix A

Atlas of interesting Events

Detector pictures of all eight events shown in figure 5.1a are presented here (three detected leptons) as well as the four events of figure 5.2c ($m_{ee} >$ 80GeV). For each event, an rz-view is shown in the left half-picture, with the particles labeled with their energies, the right half-picture shows an $r\phi$-view, with a projection of the SpaCal/BEMC or the forward LAr cells, depending on whether there was a particle detected in the forward or in the backward region. To allow a judgement of track quality, the non-vertex-fitted tracks are shown. The pictures, sorted by the invariant mass m_{12}, are labeled *(i)* to *(xii)*, numbers *(i)* to *(iv)* are from figure 5.2c, the others from figure 5.1a. Event *(iii)* is most probably background, heaved above hadronic and isolation thresholds by the high e.m. energy deposited by the forward scattered particle. Table A.1 lists the eight $3e$ events, showing the transverse momenta of each particle as well as the invariant mass of the triplet, $m_{123} = m(p_\mu^1 + p_\mu^2 + p_\mu^3)$, ranging up to 154 GeV. For each event, run and event number is given in the top left corner and the date (in a *dd/mm/yy* format) in the top right corner.

	run/event	$p_{\perp 1}$/ GeV	$p_{\perp 2}$/ GeV	$p_{\perp 3}$/ GeV	m_{123}/ GeV
(v)	192864/123614	23	19	15	131
(vi)	168058/42123	19	16	16	154
(vii)	156411/3382	10	10	2	58
(viii)	197122/71524	12	12	1	38
(ix)	200906/18138	9	13	2	32
(x)	126927/46058	9	11	2	45
(xi)	88704/143485	3	12	9	52
(xii)	191313/28316	2	14	17	43

Table A.1: *List of the eight trileptonic events from figure 5.1a, showing the transverse momentum of each particle as well as* m_{123}*, the invariant mass of the sum of the three four-momenta*

(i)

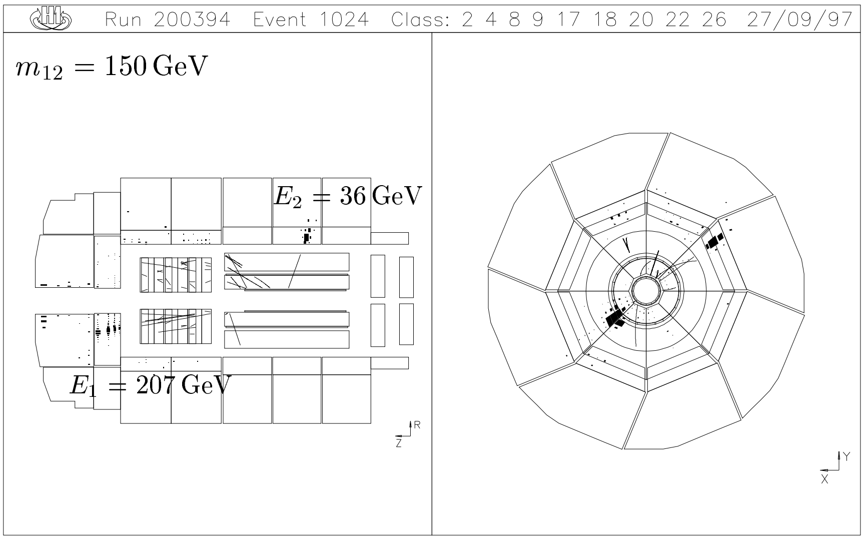

(ii)

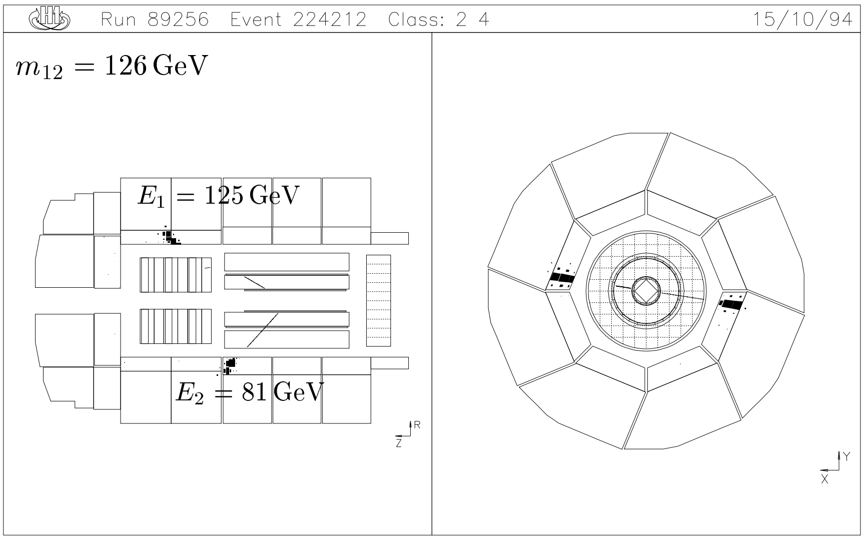
Run 89256 Event 224212 Class: 2 4
15/10/94
$m_{12} = 126\,\text{GeV}$
$E_1 = 125\,\text{GeV}$
$E_2 = 81\,\text{GeV}$
R
Z
Y
X

(iii)

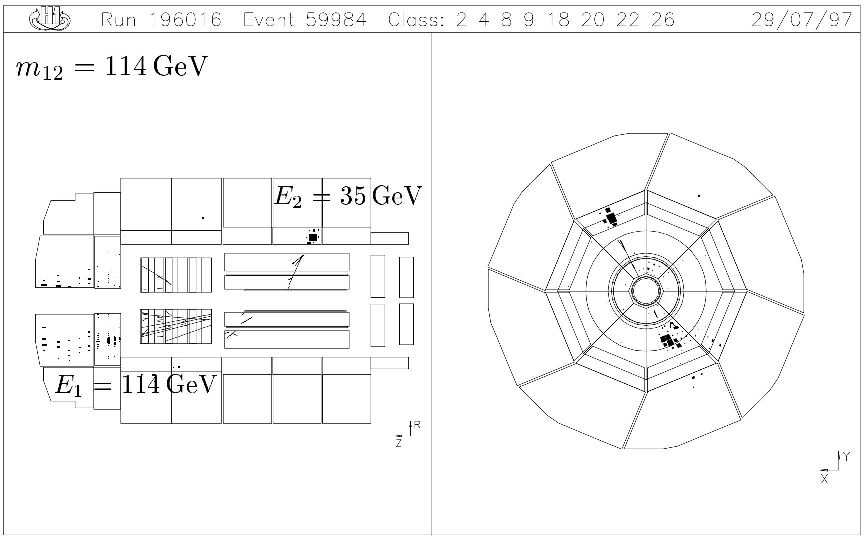
Run 196016 Event 59984 Class: 2 4 8 9 18 20 22 26
29/07/97
$m_{12} = 114\,\text{GeV}$
$E_2 = 35\,\text{GeV}$
$E_1 = 114\,\text{GeV}$
R
Z
Y
X

(iv)

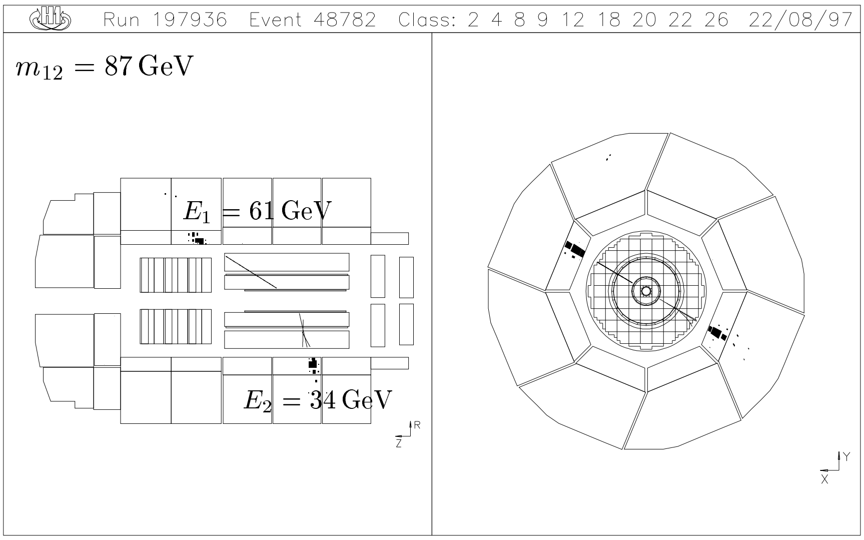
Run 197936 Event 48782 Class: 2 4 8 9 12 18 20 22 26 22/08/97
$m_{12} = 87\,\mathrm{GeV}$
$E_1 = 61\,\mathrm{GeV}$
$E_2 = 34\,\mathrm{GeV}$
R
Z
Y
X

(v)

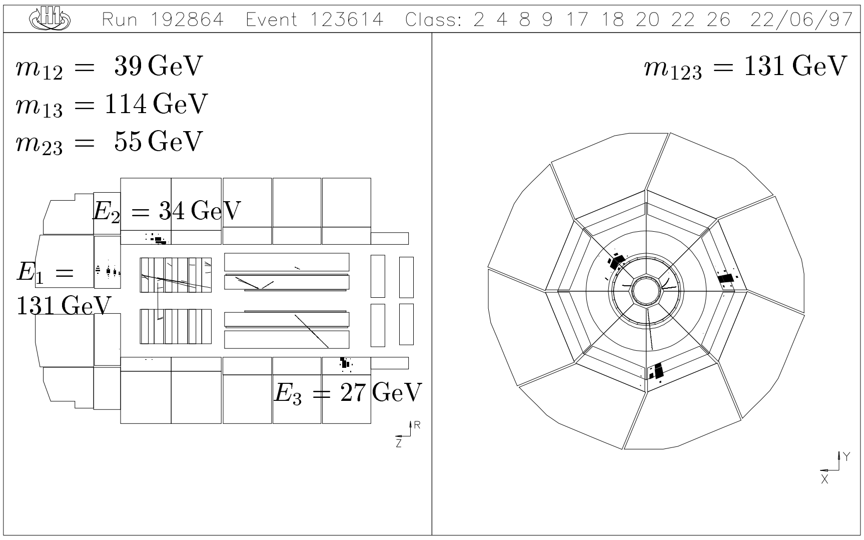
Run 192864 Event 123614 Class: 2 4 8 9 17 18 20 22 26 22/06/97
$m_{12} = 39\,\mathrm{GeV}$
$m_{13} = 114\,\mathrm{GeV}$
$m_{23} = 55\,\mathrm{GeV}$
$m_{123} = 131\,\mathrm{GeV}$
$E_2 = 34\,\mathrm{GeV}$
$E_1 = 131\,\mathrm{GeV}$
$E_3 = 27\,\mathrm{GeV}$
R
Z
Y
X

(vi)

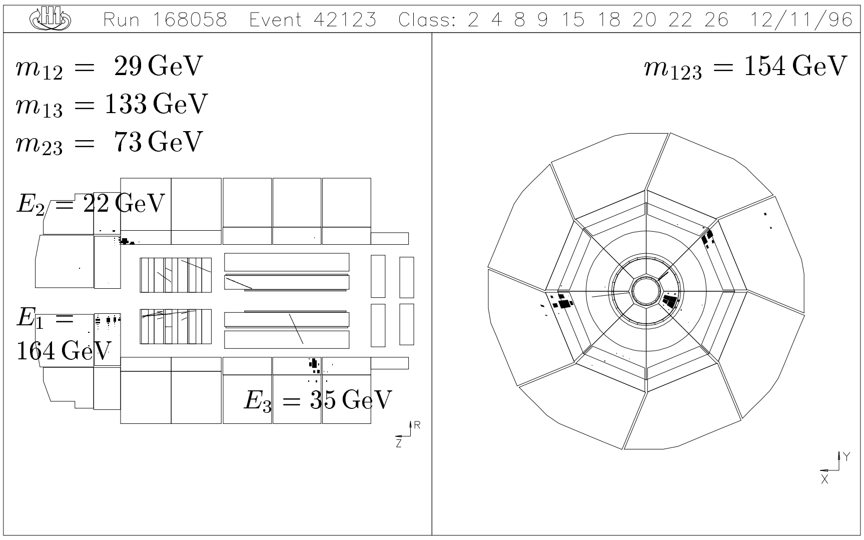
Run 168058 Event 42123 Class: 2 4 8 9 15 18 20 22 26 12/11/96
$m_{12} = 29\,\mathrm{GeV}$
$m_{13} = 133\,\mathrm{GeV}$
$m_{23} = 73\,\mathrm{GeV}$
$E_2 = 22\,\mathrm{GeV}$
$E_1 = 164\,\mathrm{GeV}$
$E_3 = 35\,\mathrm{GeV}$
R
Z
$m_{123} = 154\,\mathrm{GeV}$
Y
X

(vii)

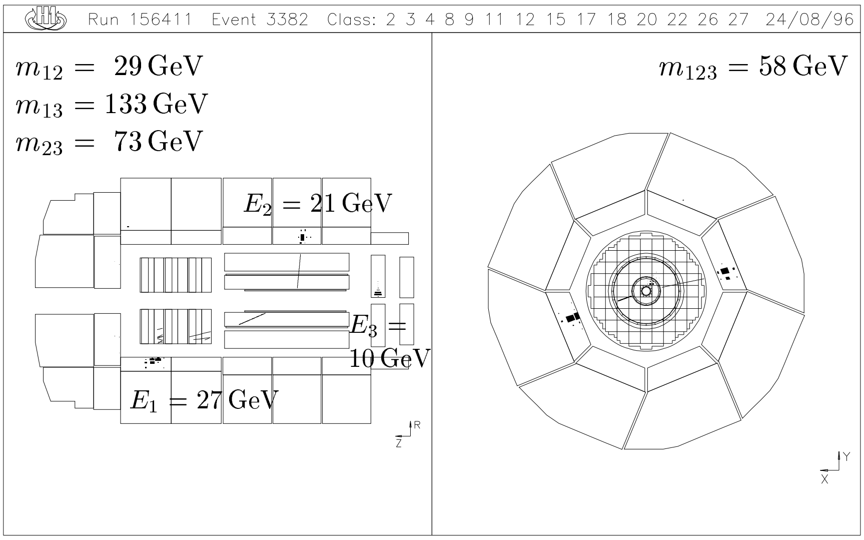
Run 156411 Event 3382 Class: 2 3 4 8 9 11 12 15 17 18 20 22 26 27 24/08/96
$m_{12} = 29\,\mathrm{GeV}$
$m_{13} = 133\,\mathrm{GeV}$
$m_{23} = 73\,\mathrm{GeV}$
$E_2 = 21\,\mathrm{GeV}$
$E_3 = 10\,\mathrm{GeV}$
$E_1 = 27\,\mathrm{GeV}$
R
Z
$m_{123} = 58\,\mathrm{GeV}$
Y
X

(viii)

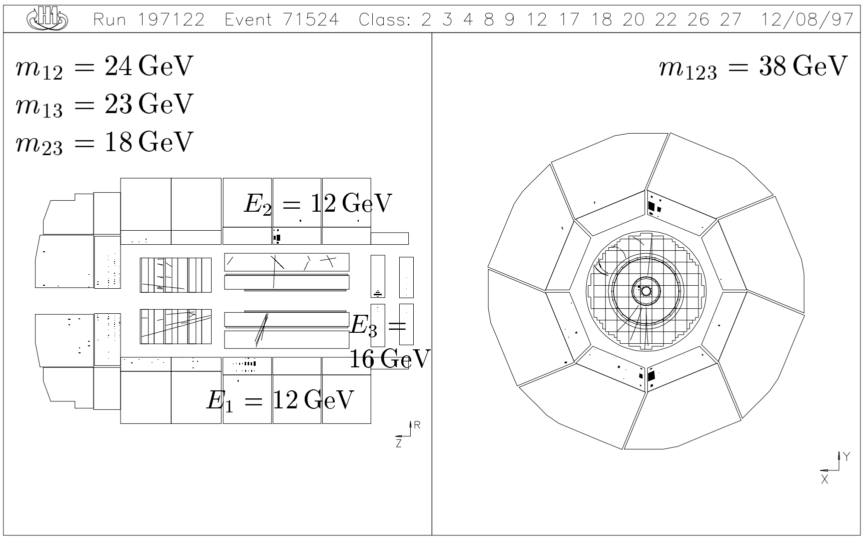
Run 197122 Event 71524 Class: 2 3 4 8 9 12 17 18 20 22 26 27 12/08/97
$m_{12} = 24\,\mathrm{GeV}$
$m_{13} = 23\,\mathrm{GeV}$
$m_{23} = 18\,\mathrm{GeV}$
$m_{123} = 38\,\mathrm{GeV}$
$E_2 = 12\,\mathrm{GeV}$
$E_3 = 16\,\mathrm{GeV}$
$E_1 = 12\,\mathrm{GeV}$
R
Z
Y
X

(ix)

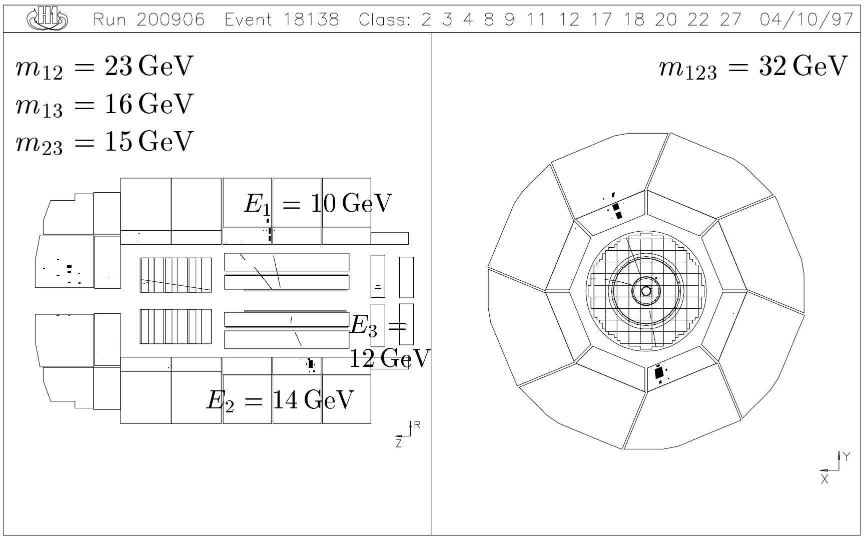
Run 200906 Event 18138 Class: 2 3 4 8 9 11 12 17 18 20 22 27 04/10/97
$m_{12} = 23\,\mathrm{GeV}$
$m_{13} = 16\,\mathrm{GeV}$
$m_{23} = 15\,\mathrm{GeV}$
$m_{123} = 32\,\mathrm{GeV}$
$E_1 = 10\,\mathrm{GeV}$
$E_3 = 12\,\mathrm{GeV}$
$E_2 = 14\,\mathrm{GeV}$
R
Z
Y
X

(x)

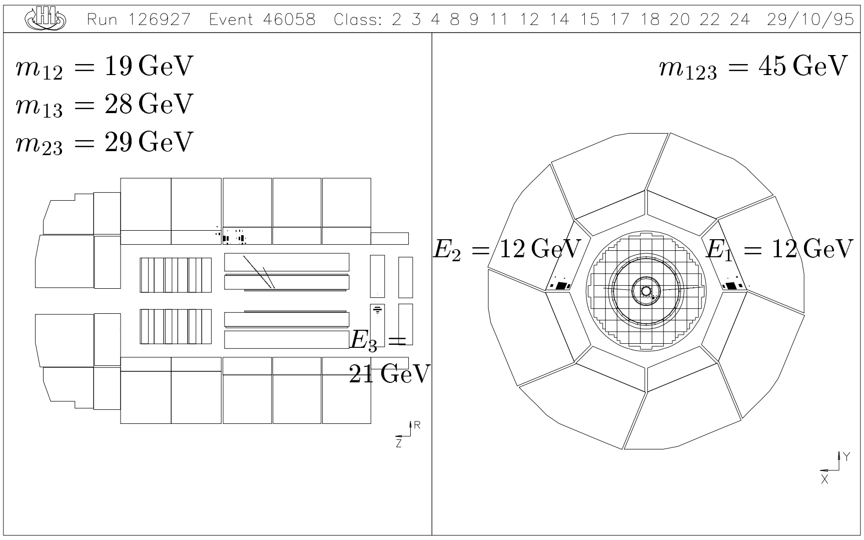
Run 126927 Event 46058 Class: 2 3 4 8 9 11 12 14 15 17 18 20 22 24 29/10/95
$m_{12} = 19\,\mathrm{GeV}$
$m_{13} = 28\,\mathrm{GeV}$
$m_{23} = 29\,\mathrm{GeV}$
$m_{123} = 45\,\mathrm{GeV}$
$E_2 = 12\,\mathrm{GeV}$
$E_1 = 12\,\mathrm{GeV}$
$E_3 = 21\,\mathrm{GeV}$
R
Z
Y
X

(xi)

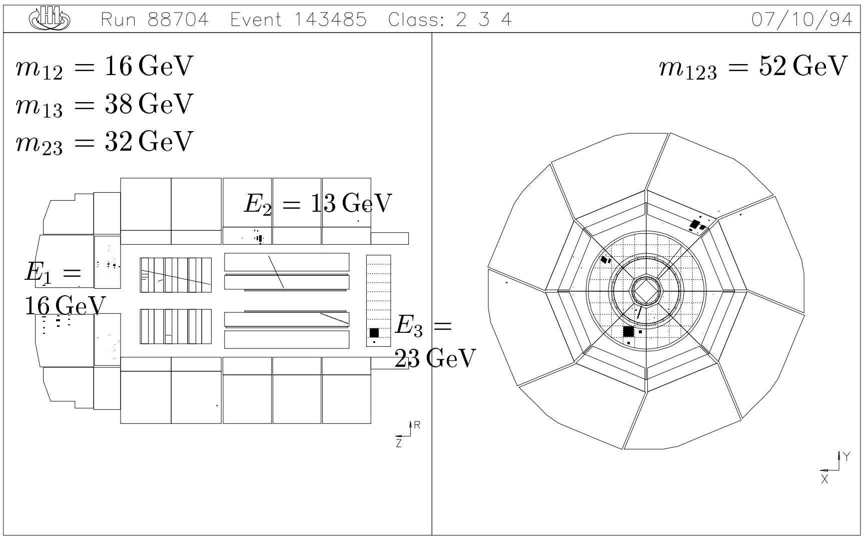
Run 88704 Event 143485 Class: 2 3 4 07/10/94
$m_{12} = 16\,\mathrm{GeV}$
$m_{13} = 38\,\mathrm{GeV}$
$m_{23} = 32\,\mathrm{GeV}$
$m_{123} = 52\,\mathrm{GeV}$
$E_2 = 13\,\mathrm{GeV}$
$E_1 = 16\,\mathrm{GeV}$
$E_3 = 23\,\mathrm{GeV}$
R
Z
Y
X

(xii)

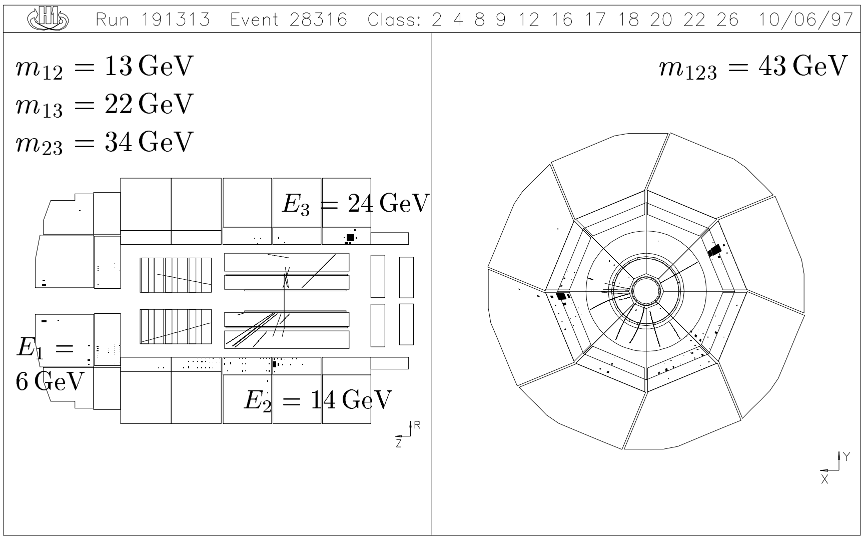
Run 191313 Event 28316 Class: 2 4 8 9 12 16 17 18 20 22 26 10/06/97
$m_{12} = 13\,\mathrm{GeV}$
$m_{13} = 22\,\mathrm{GeV}$
$m_{23} = 34\,\mathrm{GeV}$
$E_3 = 24\,\mathrm{GeV}$
$E_1 = 6\,\mathrm{GeV}$
$E_2 = 14\,\mathrm{GeV}$
R
Z
$m_{123} = 43\,\mathrm{GeV}$
Y
X

Bibliography

[1] Particle Data Group, Review of Particle Physics, *Europ. Phys. Jour.* **C3**, 1 (1998), *http://www.cern.ch/pdg/*

[2] G. Altarelli, The status of the Standard Model, *hep-ph/9710434* (1997).

[3] Steven Weinberg, The Quantum Theory of Fields, *Cambridge Univ. Press* (1995).

[4] H1 Collaboration, Observation of Events at Very High Q^2 in *ep* Collisions at HERA, *DESY 97-24; Z. Phys.* **C74**, 191 (1997).

[5] G. Altarelli et al., Pursuing interpretations of the HERA large Q^2 data, *hep-ph/9703276* (1997).

[6] J. Ellis, Hunting Down Interpretations of the HERA Large Q^2 Data, *hep-ph/9712340* (1997).

[7] H1 Collaboration, Observation of Events with an Isolated High Energy Lepton and Missing Transverse Momentum at HERA, *DESY 98-063* (1998).

[8] The H1 detector at HERA, *Nucl. Instr. & Meth.* **A386**, 310-347 (1997).

[9] Desy in Focus, *http://www.desy.de/pr-info/desy-fokus_e.html*

[10] H. Bethe, W. Heitler, *Proc. Roy. Soc.* **A146**, 83 (1934).

[11] G. Müller, A Spaghetti Calorimeter for the H1 Detector, *5th Int. Conf. on Calorimetry in HEP* (1994).

[12] H1 SpaCal Group, Performance of an Electromagnetic Lead/Scintillating-Fibre Calorimeter for the H1 Detector, *DESY Red Report 95-165, Nucl. Inst. & Meth.* **A374**, 149-156 (1996).

[13] A. Panitch, Measurement of the Proton Structure Function with H1, *Dissertation, Univ. Libre de Bruxelles* (1996).

[14] H1 software manuals, *http://www-h1.desy.de/icas/imanuals/*

[15] H1 C++ page, *http://www-h1.desy.de/icas/Cpp/*

[16] S. P. Baranov et al., LPAIR – A Generator for Lepton Pair Production, *Physics at HERA* **3**, 1478 (1991).

[17] T. Abe, GRAEPIA, *HERA MC workshop* (April 1998).

[18] H.-C. Kästli, *Thesis, ETH Zürich*, to be published.

[19] K. Charchuła, G. A. Schuler, H. Spiesberger, The Monte Carlo Generator DJANGO6 (1993).

[20] A. Schöning, Prozesse mit virtuellen und reellen $W^{\pm}$-Bosonen, *Dissertation, Univ. Hamburg* (1996).

[21] A. G. Frodesen, O. Skjeggestad, H. Tøfte, Probability and Statistics in Particle Physics, *Universitetsforlaget Oslo* (1979).

[22] Philippe Bruel, Recherche d'interactions au-delà du Modèle Standard à HERA, *These Univ. d'Orsay* (1998).

[23] M. Hapke, Messung des Wirkungsquerschnitts geladener Ströme in tiefinelastischer Streuung, *Dissertation, Univ. Hamburg* (1994).

[24] Petra Merkel, Untersuchung von Myonpaaren mit hoher invarianter Masse, *Diplomarbeit, Univ. Hamburg* (1996).

[25] GEANT long write-up, *CERN Program Library, W5103* (1989).

[26] V. Andreev, H1-Note, *H1-10/96-493* (1996).

[27] H1 Collaboration, Elastic Electroproduction of ρ and J/ψ Mesons at large Q^2 at HERA, *hep-ex/9602007* (1996).

[28] H1 Collaboration, Elastic and Inelastic Photoproduction of J/ψ Mesons at HERA, *hep-ex/9603005* (1996).